PCCP

PERSPECTIVE

View Article Online
View Journal | View Issue

Cite this: *Phys. Chem. Chem. Phys.*, 2022, **24**, 23980

Spatial programming of self-organizing chemical systems using sustained physicochemical gradients from reaction, diffusion and hydrodynamics

Anne-Déborah C. Nguindjel,† Pieter J. de Visser,† Mitch Winkens† and Peter A. Korevaar *

Living organisms employ chemical self-organization to build structures, and inspire new strategies to design synthetic systems that spontaneously take a particular form, *via* a combination of integrated chemical reactions, assembly pathways and physicochemical processes. However, spatial programmability that is required to direct such self-organization is a challenge to control. Thermodynamic equilibrium typically brings about a homogeneous solution, or equilibrium structures such as supramolecular complexes and crystals. This perspective addresses out-of-equilibrium gradients that can be driven by coupling chemical reaction, diffusion and hydrodynamics, and provide spatial differentiation in the self-organization of molecular, ionic or colloidal building blocks in solution. These physicochemical gradients are required to (1) direct the organization from the starting conditions (*e.g.* a homogeneous solution), and (2) sustain the organization, to prevent it from decaying towards thermodynamic equilibrium. We highlight four different concepts that can be used as a design principle to establish such self-organization, using chemical reactions as a driving force to sustain the gradient and, ultimately, program the characteristics of the gradient: (1) reaction–diffusion coupling; (2) reaction–convection; (3) the Marangoni effect and (4) diffusiophoresis. Furthermore, we outline their potential as attractive pathways to translate chemical reactions and molecular/colloidal assembly into organization of patterns in solution, (dynamic) self-assembled architectures and collectively moving swarms at the micro-, meso- and macroscale, exemplified by recent demonstrations in the literature.

Received 4th June 2022,
Accepted 15th September 2022

DOI: 10.1039/d2cp02542f

rsc.li/pccp

1. Introduction

The spontaneous emergence of shape, structure and patterns is one of the most fascinating processes in life.[1,2] At small length scale, a living cell combines a vast amount of molecular building blocks into functional architectures, for example the cytoskeleton that enables the cell to move and divide.[3] Primitive unicellular organisms employ the cytoskeleton to achieve highly dynamic shape transformations at the macroscale. For example, *Physarum polycephalum* slime molds self-organize into networks to explore their surroundings, and reconfigure to optimize food acquisition and distribution.[4] Social amoebae *Dictyostelium discoideum* colonies collectively aggregate from a dynamic swarm of individually moving cells into fruiting bodies,[5] and multicellular organisms generate structures of increasing complexity over the course of embryonic development.[6] Importantly, the bottom-up emergence of functional structures in life is entirely driven by chemical and physical principles, which transduce molecular interactions into structures at length scales well beyond the molecular building blocks. Recreating such self-organization – spontaneous emergence of patterns and structures as directed by internal processes, rather than external control – from integrated chemical reactions, assembly pathways and physicochemical phenomena is one of the biggest fundamental challenges in systems chemistry.[7–10] To this end, *de novo*-designed chemical systems based on a minimalistic set of elements allow us to elucidate the general principles that are essential for self-organization of supramolecular structures, crystals, colloids and soft matter. At the same time, these insights offer new potential in novel classes of synthetic matter that display 'life-like' behaviour, *i.e.* operate autonomously and interact with cues from their environment. Bottom-up control in such systems will allow them to morph into functional structures, adapt to changing circumstances, and ultimately enable intelligent systems with potential in *e.g.* diagnostics, interactive biomaterials or molecular computing.

Non-covalent, reversible associations embedded in the design of the building blocks provide a powerful tool to program

Institute for Molecules and Materials, Radboud University, Nijmegen, The Netherlands. E-mail: p.korevaar@science.ru.nl
† These authors contributed equally.

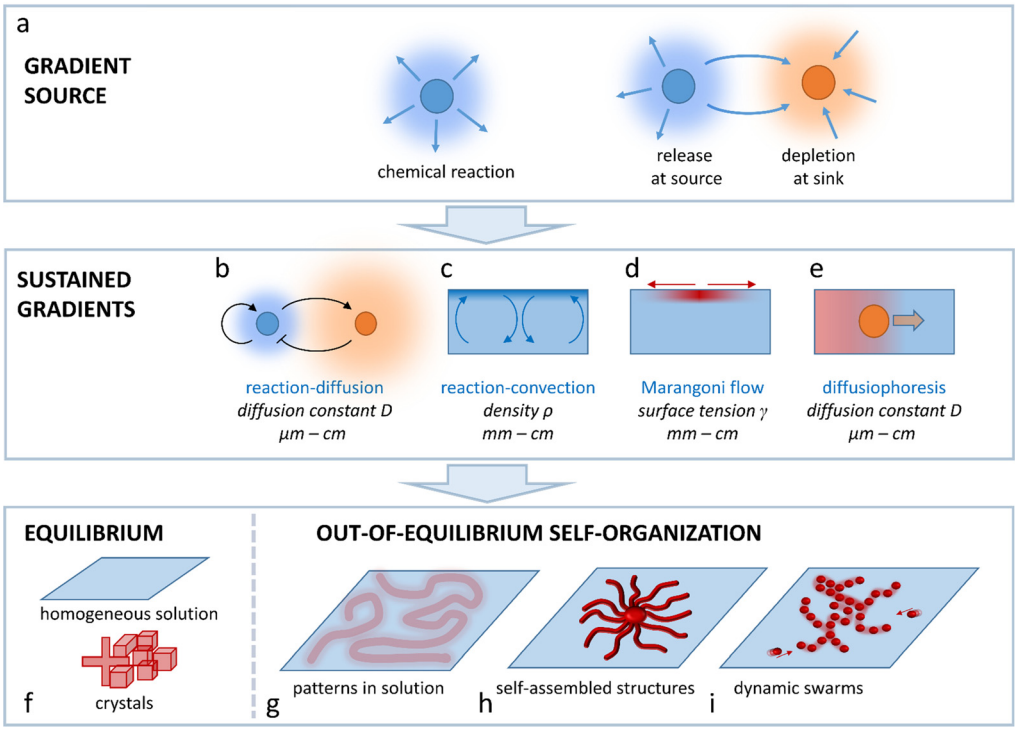

Fig. 1 Spatial programmability in self-organization *via* sustained physicochemical gradients. (a) The gradient is first produced *via* a chemical reaction, release or depletion of a compound. The gradient then needs to be transduced into a sustained pattern, *via* (b) reaction–diffusion coupling, (c) reaction–convection, (d) the Marangoni effect or (e) diffusiophoresis. (f) Whereas building blocks (molecules, colloids) form either a homogeneous solution or static structures under equilibrium conditions, sustained gradients result in out-of-equilibrium self-organization of (g) patterns in solution, (h) self-assembled structures or (i) dynamic swarms.

assembly processes. Under thermodynamic control, the assemblies will spread out into a homogeneous solution, or form equilibrium structures, such as supramolecular assemblies or crystals (Fig. 1). Developing 'life-like' systems however involves a paradigm where self-organization occurs out-of-equilibrium.[11–15] For example, the construction of the cells' cytoskeleton shows how coupling of assembly steps to chemical reactions drives self-organization in time and space.[16] First, the tubulin building blocks are activated by a chemical fuel, guanosine triphosphate (GTP), in order to assemble into microtubules. Over time, hydrolysis of GTP occurs, and tubulin becomes inactive again. Hence, the self-organization of the microtubules relies on the supply of fresh GTP, which enables the cell to control the build-up and disassembly of the cytoskeleton. The transient nature of microtubule assemblies has inspired the development of synthetic systems[17,18] – varying from 1D nanofibers[19–23] to colloidal assemblies[24] and macroscale gels[25] – that form and fall apart over time, as programmed by the kinetics of the underlying chemical reactions.

This Perspective addresses the challenge to arrive at spatial programmability in the out-of-equilibrium organization of matter that is of interest to systems chemistry, ranging from supramolecular assemblies to colloids, hydrogels, crystalline structures and flow patterns in chemical reaction networks. In general, such organization requires the spontaneous emergence of concentration gradients that provide a spatial differentiation in the system. To avoid decay back to thermodynamic equilibrium (*e.g.* a homogeneous solution, emulsion, or non-organized dispersion of colloids), these gradients need to be sustained under out-of-equilibrium conditions. Such sustainment requires at first a gradient source; a chemical reaction that takes place in solution, a source element that releases a chemical compound, or a sink element that depletes the compound. Even though patterns can emerge around gradient sources that are *a priori* localized at a fixed position, in an entirely self-organizing system, one needs a mechanism by which the production, release or depletion of the compound gets localized such, that the gradient of this compound is sustained. In this Perspective, we outline four physicochemical principles that enable design strategies to arrive at sustained gradients in solution-based systems: reaction–diffusion coupling (Fig. 1b), reaction–convection (Fig. 1c), the Marangoni effect (Fig. 1d) and diffusiophoresis (Fig. 1e). We selected these principles as they provide unique pathways to direct the self-organization of systems that either comprise concentration patterns in solution (Fig. 1g), self-assembled structures (Fig. 1h) or dynamic swarms of colloids or (micro)-droplets (Fig. 1i), at the micro-, meso- or macroscale.

2. Reaction–diffusion systems

The coupling of chemical reactions and diffusion lends itself towards the construction of self-organizing systems. In nature, pattern formation in processes such as embryonic development

has been rationalized by two concepts, which may take place in conjunction: Wolpert's positional information, and Turing instability.[26–29] In Wolpert's concept, gradients of chemicals (morphogens) are locally amplified to establish spatial differentiation, dividing the area in which the gradient is present into multiple zones with large differences in terms of chemical composition (Fig. 2a). This is accomplished by local regulatory interactions, which rely on gene networks that combine repression, (auto)activation and cross-regulation of multiple genes. In Turing's mechanism, a homogeneous system spontaneously generates patterns with repetitive structure.[12,30–35] These Turing patterns can be achieved *via* as little as two components; the activator which promotes the production of both components (positive feedback), and the inhibitor which inhibits the production of the activator (negative feedback) and has a high diffusion rate compared to the activator (*i.e.* $D_a \ll D_i$, Fig. 2b). Starting off from a homogeneous solution with activator and inhibitor, even the slightest local increase in the activator concentration (1) amplifies both the local activator and inhibitor concentration in a self-sustaining fashion (2). While the peak in activator concentration remains localized due to its low D_a, the inhibitor rapidly diffuses away from the activation site, suppressing production of the activator in neighboring areas (3). Outside of this area, new peaks in activator concentration eventually arise (4). Finally, the entire solution is divided into a periodic pattern of high and low activator concentration, their spacing regulated by the combination of reaction and diffusion kinetics inherent to the chemical network (5).

The first experimental demonstration of a Turing pattern in a synthetic system was provided by Castets *et al.* in the chlorite-iodide-malonic acid (CIMA) reaction, where starch, used as indicator in the gel, provides a selective complexation and thereby generates the required distinction in diffusion rates between the activator (iodide) and the inhibitor (chlorite).[36–39] Furthermore, Turing patterns have been reported in the ferrocyanide–iodate–sulphite reaction[40–42] and, under specific conditions, in the Belousov–Zhabotinsky (BZ) reaction.[43–45] In this reaction that naturally displays reaction–diffusion patterns, oscillation results from the autocatalytic oxidation of a redox catalyst by bromate ions (activator), a process that is inhibited by bromide ions. A reducing agent (*e.g.* malonic acid) restarts the cycle, by reducing the catalyst again. Classically, the BZ reaction provides waves at the cm-scale that spiral through the reaction medium in an unstirred batch configuration. However, Epstein *et al.* showed how the classical BZ reaction can be further tailored in water-in-oil micro-emulsions.[46,47] Here, differentiation in diffusivity is obtained as polar species are transferred *via* the aqueous micro-droplets, whereas non-polar intermediates are transferred more rapidly as they diffuse through the oil-based continuous phase, resulting into a large diversity of spatial organizations, including Turing patterns in the 100 micrometer-range.[48]

Even though most of these pattern-forming reactions are found by chance,[49] it is clear that the emergence of reaction–diffusion patterns relies on the kinetic reaction rate constants and diffusion constants involved,[41,50,51] and various models have been developed to simulate reaction–diffusion patterns.[11,52–55] Furthermore, generic design principles have been proposed, such as a stepwise method through which an oscillatory reaction occurring in a homogeneous, well-mixed solution can be

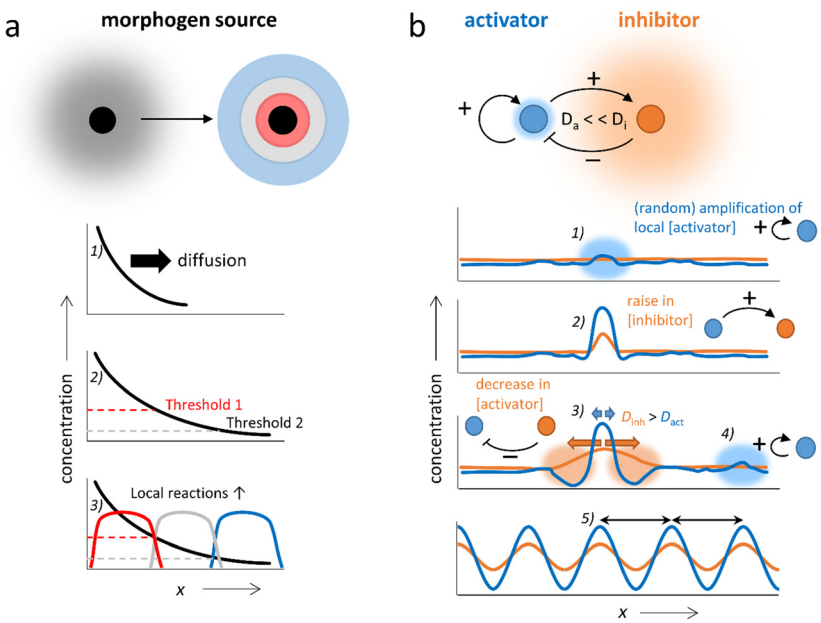

Fig. 2 The two main theories behind pattern formation in nature. (a) Wolpert's positional information. (1) A morphogen gradient spreads from a source by diffusion. (2 and 3) Chemically distinct zones are then created by local reactions as determined by threshold concentrations. For three zones, this is known as a 'French flag pattern'. (b) Turing instability: (1, 2) autocatalytic enhancement of (random) fluctuations creates a local peak in both activator and inhibitor concentration. (3) Because $D_a \ll D_i$, the inhibitor diffuses outward, depressing nearby activator concentration, while the activator peak sustains itself. (4, 5) As more and more peaks emerge from new fluctuations, synchronization occurs naturally as depression zones overlap.

translated into reaction–diffusion patterns in open one-side-fed reactors.[56,57] To this end, a complexing agent is introduced which selectively binds the activator to decrease its diffusion rate (a strategy that was suggested earlier by Lengyel and Epstein[38]), as well as an antagonist reaction to control its accumulation. All in all, examples of complexity emerging from reaction–diffusion systems have been demonstrated which range from nano- and microscale structures to patterns that span centimeters, and from "static" Turing patterns to dynamic patterns that continuously change over time.[49,58–63] Here, we highlight some of the more recent strategies that have been developed to couple reaction and diffusion and generate self-organizing structures and patterns.

2.1 Reaction–diffusion systems as a means to create complex structure

First, we discuss approaches to self-organize complex static structures with distinct topologies and functionalities that are otherwise difficult to achieve. Recently, Wu *et al.* reported the synthesis of Cu^{2+}-loaded Turing membranes, which improve ionic conductivity in zinc-based batteries.[64] To create these membranes, a homogeneous solution of polybenzimidazole (PBI) is cast in a thin film on a substrate, and immersed in a $CuCl_2$ solution in *N*,*N*-dimethylacetamide (DMAc) (Fig. 3a and b). Cu^{2+} ions dissociate from the DMAc solvent, and coordinate with the pyridine moiety in the PBI polymer chains. The PBI–Cu^{2+} complex now functions as the activator for the membrane formation, as further diffusion of reactants towards the activated site is accelerated by local depletion of PBI and Cu^{2+}, generating a cross-linked polymer network. At the same time, DMAc molecules that are released from Cu^{2+} ions that have been associated to PBI diffuse away from the active site – much faster than the PBI–Cu^{2+} complex. Thereby, DMAc functions as an inhibitor, and sequesters Cu^{2+} at neighboring locations where PBI–Cu^{2+} has not formed yet. Together, the PBI–Cu^{2+} activator and DMAc inhibitor generate Turing patterns of PBI–Cu^{2+}: the crests and troughs that emerge in the initially homogeneous PBI-film have a typical feature size of approximately 100 μm.

Furthermore, inorganic structures with biomorphic shapes such as corals, vases and helices can be generated upon coupling the precipitation reactions of barium carbonate ($BaCO_3$) nanocrystals and amorphous silica (SiO_2). García-Ruiz showed how polycrystalline biomorphic structures grow when CO_2 diffuses into an aqueous solution of sodium metasilicate (Na_2SiO_3) and barium chloride ($BaCl_2$).[65,66] These chemicals participate in the following (overall) precipitation reactions:

$$Ba^{2+} + CO_2 + H_2O \rightarrow BaCO_3 + 2H^+ \quad (1)$$

$$SiO_3^{2-} + 2H^+ \rightarrow SiO_2 + H_2O \quad (2)$$

The diversity of biomorphic structures that can be formed relies on the non-linear behavior of the reaction–diffusion systems that emerge from these coupled reactions, due to their pH-dependent – and pH-altering characteristics; concentration gradients of protons and ions at the growth front, and the poisoning of silica precipitates on $BaCO_3$ crystal growth, which in turn affects the growth-direction of the nanocrystals.[67,68]

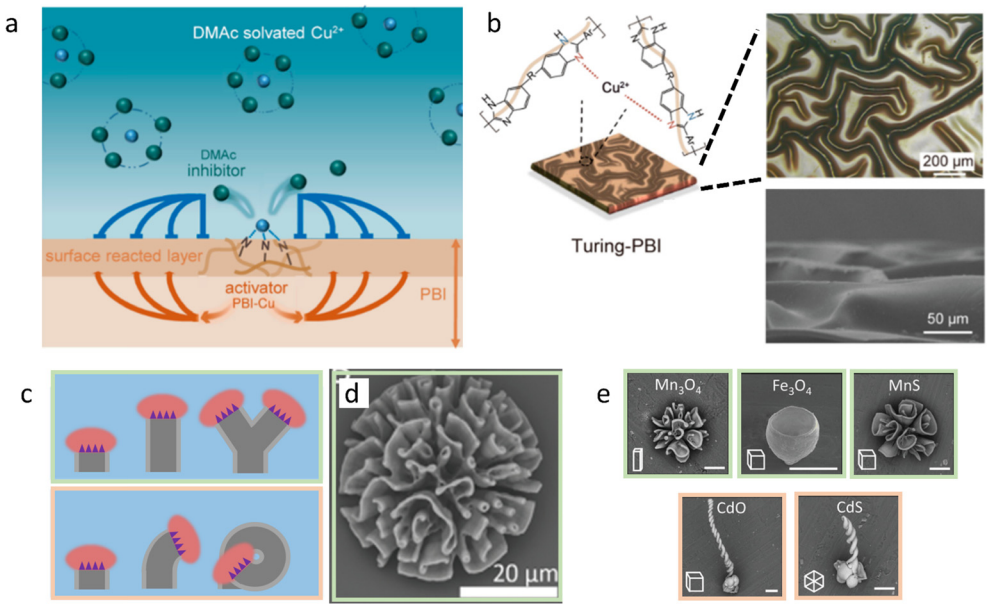

Fig. 3 Complex static structures emerge from reaction–diffusion. (a) DMAc functions as the inhibitor in a Turing-like reaction–diffusion system, resulting in patterned PBI-Cu membranes (b). Reprinted (adapted) with permission from ref. 64. Copyright 2021 American Chemical Society. (c) Various polycrystalline biomorphic structures grow from reaction–diffusion triggered $BaCO_3$–SiO_2 co-precipitation. Due to the narrow pH range in which passivating SiO_2 precipitation takes place, crystal formation is affected by the acidic growth front. This causes the structures to 'blossom' towards the bulk solution if it has high pH (top) and 'curl' inwards if bulk pH is lower (bottom). (d) $BaCO_3$–SiO_2 co-precipitate structure that is formed in the blossoming regime. (e) Ion-substituted structures, exemplifying the shapes obtained in either the blossoming (top row) or curling (bottom row) regime. Reproduced from ref. 72 with permission from the Wiley-VCH publishing group, Copyright 2020.

Noorduin *et al.* exploited the mutual feedback between $BaCO_3$ precipitation, which decreases the pH, and SiO_2 precipitation, which takes place in a narrow pH range, in order to create a reaction–diffusion scenario.[69,70] In the pH and concentration ranges they explored, distinct growth regimes can be accessed by tuning the pH of the bulk solution. In the 'blossoming' regime (Fig. 3c top), the pH of the bulk solution is high, such that proton release resulting from $BaCO_3$ precipitation puts the local pH at the upper boundary for SiO_2 precipitation, that would passivate the crystal growth. Hence, the growth front progresses towards the bulk solution, such that the pH at the growth front remains *above* the range for silica precipitation, resulting into stems, cones and coral like structures (Fig. 3d). In the 'curling' regime (Fig. 3c bottom), the pH of the bulk solution is slightly lower and acidification by $BaCO_3$ precipitation puts the local pH at the lower boundary for SiO_2 precipitation. The local pH at the growth front is below the pH range for silica precipitation, whereas the bulk pH is within this range. Hence, any growth towards the bulk will enter the SiO_2 precipitation regime; the structures will therefore only grow away from the bulk solution, either by forming flat sheets along the interface, or by curling along each other. Changing the environmental conditions by *e.g.* changing the CO_2 influx, or the local availability of CO_2 *via* a photochemical reaction,[71] allows modulating the local gradients around the growth front, and thereby switching between different types of structures that are co-precipitating over the course of the growth process. Finally, the structures produced this way can be modified *via* ion-exchange reactions (Fig. 3e), to function as selective catalysts or translocate under the influence of a magnetic field.[72]

2.2 Reaction–diffusion systems with sustained oscillations

In addition to static patterns, reaction–diffusion coupling can be exploited in self-organizing systems that display spatiotemporal dynamics. The BZ reaction offers an attractive pathway to translate spatiotemporally oscillating concentration gradients into (functional) responses at material-level. This reaction is unique due to its ability to sustain oscillations for hundreds of cycles in a closed system, which manifest as expanding ring-shaped pulses ('target patterns') or spirals.[73] Furthermore, inclusion of photo-responsive catalysts allows external control over the dynamics of the system *via* light exposure.[74,75]

For example, Yoshida *et al.* have exploited the BZ reaction to direct biomimetic hydrogels that are able to move without any external driving force.[76] An oscillating hydrogel was produced by including a $Ru(bpy)_3$ catalyst – which can participate in the BZ reaction – into a poly(NIPAAm-*co*-$Ru(bpy)_3$-*co*-AMPS) polymer network. Upon immersion of the gel in the catalyst-free BZ reaction medium, the BZ reaction starts and the catalyst inside the hydrogel oscillates between Ru(III) and Ru(II) oxidation states. These oxidation states, in turn, influence the hydrophilicity of the gel, and thereby drive its periodical swelling (Ru(III)) and deswelling (Ru(II)), which results into peristaltic motion of the gel (Fig. 4).[77] Alternatively, walking motion can be achieved using gels that swell asymmetrically due to an internal gradient

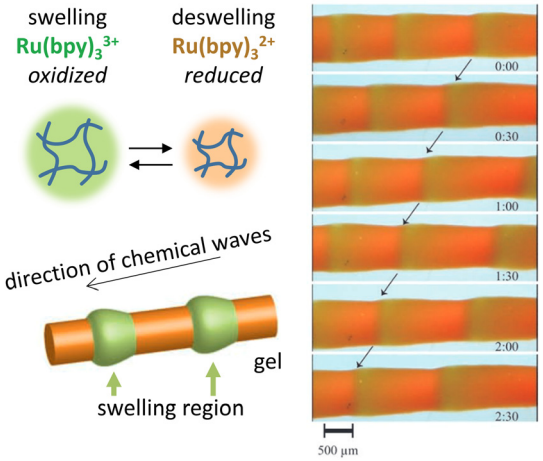

Fig. 4 Functional oscillating systems based on the Belousov–Zhabotinsky (BZ) reaction. By incorporating the BZ reaction into a hydrogel, the hydrophilicity change resulting from Ru^{2+}–Ru^{3+} switching can be exploited to cause periodic swelling and deswelling, giving rise to peristaltic motion. Reproduced from ref. 77 with permission from the Wiley-VCH publishing group, Copyright 2008.

in $Ru(bpy)_3$ and AMPS concentration, and self-oscillating polymer brushes – polymer chains grafted onto a glass substrate – can be used to transport nanoscale objects.[76,78] Using a similar poly(NiPAAm-*co*-$Ru(bpy)_3$-*co*-AMPS) hydrogel immersed in catalyst-free BZ-solution, Lu *et al.*[79] exploit the catalyst's photosensitivity. When weakly illuminated, the frequency of oscillations in the gel increases with light intensity, while above a certain intensity threshold, stronger illumination reduces the oscillation frequency instead. When placed inside a capillary of which the left and right halves are illuminated with different intensities, the authors were able to cause both photophobic and phototropic motion of the gel, as the imbalance between oscillation frequencies in the weakly and brightly illuminated parts of the gel dictated its movement.

Additionally, BZ reactions can be used as a basis for chemical communication amongst compartmentalized systems such as micro-droplets or -particles.[80–82] For example, Litschel *et al.* used this concept to create a synthetic 'central pattern generator', a motif found in the nervous system that produces pulses which alternatively travel down the left and right sides of its spinal column, inducing cyclic muscle contractions.[83] A microfluidic device was created that comprises a linear array of nanoliter wells, connected *via* microchannels and loaded with the BZ reagent solution. Coupling of the BZ reactions in neighboring wells occurs either by diffusion of the hydrophobic inhibitor Br_2 through the PDMS walls (inhibitory coupling), or by water-soluble species, which can propagate oscillations along the microchannels (excitatory coupling). A photosensitive catalyst was included to suppress spontaneous oscillation by initially exposing the wells to light. As a result, BZ oscillations selectively start when the light is turned off at the beginning of the array (the 'pacemaker'), which excites the subsequent wells, such that traveling waves of BZ oscillations progress down the array. Even if the two parallel arrays are excited simultaneously,

their inhibitory coupling upon exchange of Br_2 through the PDMS walls causes a phase-shift, such that they end up oscillating out of phase. One can envision such a system being coupled to previously mentioned examples of contracting BZ-gels, creating synthetic analogues of muscles that constantly contract and relax upon actuation by neural signals.

2.3 *In vitro* reaction–diffusion systems based on biomolecules

The impressive complexity that can be established from chemical systems such as the BZ reaction – which relies on a fixed reaction network topology – has inspired the bottom-up design of reaction networks based on biomolecules. The sequentially programmable nature of DNA strands allows precise control over the topology of the reaction network and thereby reaction and diffusion rates. As a result, it becomes possible to translate the high degree of control inherent to DNA programming into macroscale spatial patterns and sustained out-of-equilibrium gradients. This concept has been exploited by various research groups,[84–88] who implemented toehold-mediated DNA strand displacement reactions into reaction–diffusion networks. Such reactions require a partially hybridized complex of two DNA strands, to which a single complementary DNA strand is then added as an input. This input strand now displaces one of the original (partly bound) DNA strands, which is released as the output – a reaction that is driven by the gain in number of hydrogen bonds. The release of the output strands can be followed by functionalizing them with a fluorescent probe that is inactive when in close contact to a quencher in the DNA hybrid, and displays strong fluorescence when the output strand is free in solution.

For example, Chen *et al.* reported a system where rapidly diffusing activator (input) strands displace fluorescent signal strands from reporter hybrids.[84] Subsequently, the signal strands can be sequestered by slowly diffusing inhibitor hybrids. Various fluorescent patterns can then be generated from gels with a homogeneous loading of these reporter hybrids. For example, single and concentric rings spread outward from a cavity in the gel that contains both activator and inhibitor strands, while destructive interference patterns appear when one cavity is filled with activator and another with inhibitor, and constructive interference is observed when orthogonal activators are added into separate cavities. Zenk *et al.* reported a setup that generates sustained DNA concentration gradients and patterns.[85] In their design, single and double DNA strands diffuse from opposite liquid reservoirs into a hydrogel, and release an output DNA strand *via* strand-displacement. Throughout the system, 'recapturer complexes' are present at constant concentration in order to sequester the output strands. Together, this constant production and depletion of the output strands maintains a stable, yet out-of-equilibrium concentration profile in the hydrogel. This approach provides the foundation for the experimental realization of (programmed) DNA-based pattern generating systems which thus far have only been demonstrated *in silico*, such as the pattern-processing modules used by Scalise *et al.* in their simulations.[86]

In addition to these DNA strand displacement reactions, Zadorin *et al.* have demonstrated how positional information can be established in DNA-based systems with chemical reactions that produce and deplete DNA strands.[87] In the example highlighted in Fig. 5a, autocatalysis of activator DNA strand A_1 is established *via* template strand T_{A_1}. Upon binding of the activator, T_{A_1} templates the extension of A_1 into a strand that comprises two sequences of A_1 – a reaction that is catalyzed by DNA polymerase. Next, a nicking enzyme cleaves the extended strand such that two A_1 strands are released from this autocatalytic system. Finally, A_1 is converted into waste when DNA polymerase acts upon it while it is bound to repressor strand R_1. By combining autocatalysis and inhibition, a weak gradient in repressor strand can be transferred into a strong, almost

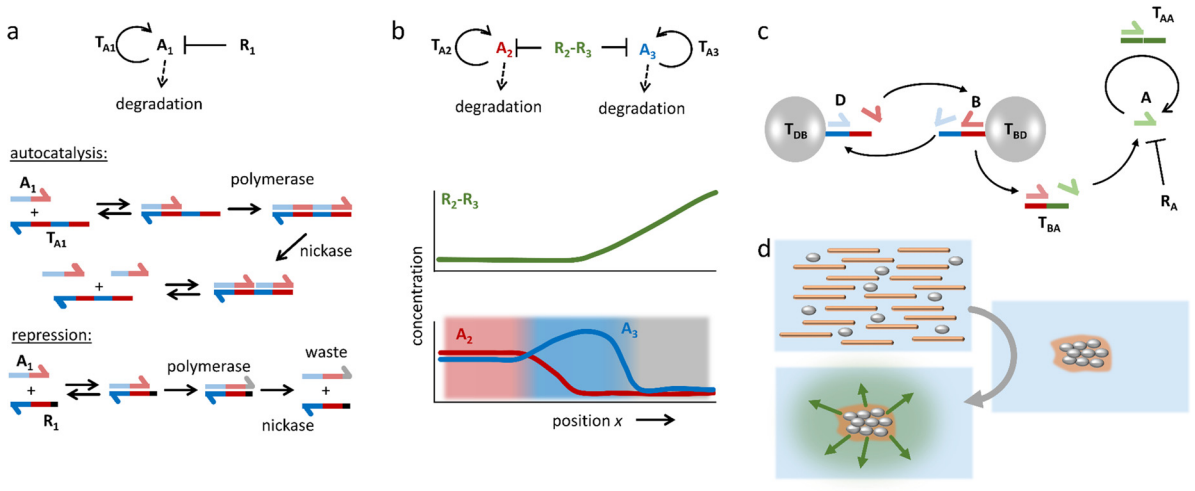

Fig. 5 DNA-based reaction–diffusion systems. (a) DNA reaction networks for autocatalysis, repression and degradation. (b) A bifunctional repressor strand functions as the morphogen in a demonstration of DNA-based positional information. The repressor gradient is amplified by the autocatalytic reactions, resulting in three zones with distinct chemical compositions, *i.e.* a 'French flag pattern'.[87] (c) A DNA-based density-dependent autocatalytic reaction is triggered as a network of beads, microtubules and kinesin motors contracts. (d) As a result, a fluorescent front is initiated from the sites where a critical bead density is reached.[88]

stepwise increase in A_1 concentration – in analogy to Wolpert's scenario – with the repressor R_1 functioning as the morphogen. By coupling two orthogonal autocatalytic motifs *via* a morphogen that contains both repressor strands, a 'French flag pattern' with three chemically distinct zones can be generated based on a single morphogen gradient (Fig. 5b). This gradient is then exploited to selectively bind colloidal beads in a particular area *via* DNA hybridization.

Self-organization processes in life, such as embryonic development, often involve a coupling of chemical as well as mechanical systems. Such coupling can pave the way towards new control mechanisms in artificial self-shaping materials. In work by Senoussi *et al.*, DNA reaction networks were implemented in active matter-based gels that, upon contraction, initiate propagating reaction fronts.[88] To this end, two different types of microbeads are functionalized at their surface, each with one type of single DNA strand, where bead type B templates the formation of the activator for bead type D, and *vice versa* (Fig. 5c). These beads are loaded into a solution with an activator strand-degrading exonuclease, as well as microtubules and kinesin motors, which together form an active gel that concentrates the microbeads upon contraction. When the microbeads are brought close together, they easily exchange their activator strands in cross-catalysis. Next, activator species B is coupled to a motif (T_{BA}) that enables autocatalysis of activator A. As a result, an autocatalytic front of A emerges, which is triggered from the location where the active gel has started to contract (Fig. 5d).

Finally, the spatiotemporal patterns that emerge from the Min protein system provide an intriguing platform to study *in vitro* pattern formation. The Min protein system is a biological reaction–diffusion system in *Escherichia coli* that comprises the MinD and MinE proteins, and forms patterns that localize the middle plane to assist in bacteria cell division. MinD switches from a solubilized monomeric state in solution to a membrane-bound dimeric state upon binding ATP (Fig. 6a). MinD at the membrane sequesters MinE from the solution, which elevates the ATPase activity of MinD. As result ATP is hydrolyzed to ADP, and MinD dissociates from the membrane again. In the reaction–diffusion patterns that emerge from this system, MinD serves as the activator, and MinE as the inhibitor. To introduce external control, comparable to the photocatalytic BZ reactions, Glock *et al.* introduced an azobenzene-bound peptide derived from MinE. This peptide binds to MinD when the azobenzene moiety is in the *cis* state, activating its ATPase activity and thereby triggering its dissociation from the membrane (Fig. 6b).[89] Importantly, the binding and unbinding of the peptide-azobenzene derivative to MinD can be controlled by promoting the cis or trans state upon exposure to UV and blue light, respectively. Notably, entrainment of the spatiotemporal patterns of the MinDE system was obtained after periodic illumination by UV, which remained stable for more than 20 illumination cycles (Fig. 6c). When the periodic illumination was stopped, the spatiotemporal patterns returned to their ground state after a few oscillations. The relative simplicity of this network and the manipulation technique offers possibilities for control of nonlinear dynamics of natural reaction–diffusion systems. This opens pathways to establish patterns in synthetic biology contexts, such as the development of a synthetic cell.

3. Reaction–convection systems

Chemical reactions can also give rise to self-organization by affecting the local physical properties of the solution, *e.g.* generate imbalances in density or surface tension (*vide infra*).[90–93] Such chemo-hydrodynamic coupling enables simple A + B → C reactions, or even A → B reactions to drive the self-organization of concentration patterns that spontaneously emerge in an initially homogeneous solution. When buoyancy

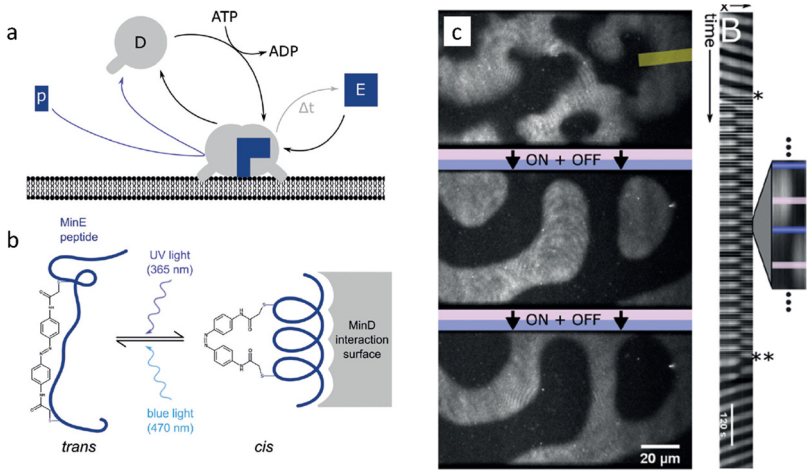

Fig. 6 Entrainment of Min-protein patterns based on a photoswitchable MinE peptide. (a) Monomeric MinD in solution forms a dimer that attaches to the membrane upon binding ATP. (b) Upon illumination with UV, the MinE peptide associates with membrane-bound MinD, causing hydrolysis of ATP followed by release of MinD from the membrane. (c) Periodic illumination of the sample synchronizes the patterns with the light pulses. Reproduced from ref. 89 with permission from the Wiley-VCH publishing group, Copyright 2018.

is the driving factor, these patterns rely on the convection patterns that are driven by local variations in the density of dissolved compounds in solution. Here, a chemical reaction produces a high-density product on top of a low-density reactant solution, or a low-density product at the bottom of a high density reactant solution, such that a convective flow emerges to negate this density instability. The high-density solution is transported downward while a counterbalancing flow is directed upward. Depending on the physical characteristics of the system, *e.g.* the fluid viscosity and liquid depth, convection patterns are generated with regions of upward and downward flow, as schematically shown in Fig. 7. Comparable convection patterns emerge in liquid systems that are heterogeneously heated, due to the well-known Rayleigh–Bénard instability. The difference between these two buoyancy driven convection phenomena is the mechanism through which the density variations arise: solutal expansion due to a chemical reaction *versus* thermal expansion due to heating.

Solutal buoyancy convection is described by the solutal Rayleigh number, the ratio between the rate of convective transport due to solutal buoyancy and the rate of diffusive transport:

$$\mathrm{Ra} = \frac{\partial \rho}{\partial c_\mathrm{p}} \frac{c_{r0} L_\mathrm{c}^3 g}{D\mu} \quad (1)$$

with ρ the solution density, c_p the concentration of the product, c_{r0} the initial reagent concentration, L_c the characteristic length scale of the system (generally the liquid depth), g the gravitational constant, D the diffusion coefficient of the product and μ the dynamic viscosity of the solution.[94] Only if Ra is larger than a critical value $\mathrm{Ra_c}$, convection patterns like flow cells can form. $\mathrm{Ra_c}$ strongly depends on the geometry and boundary conditions of the system and is hard to compute for a given experimental system.[95,96] Ra can be modulated by varying the reagent concentration c_{r0}, liquid depth L_c or liquid viscosity μ.

Importantly, if $\mathrm{Ra} \gg \mathrm{Ra_c}$, strong convection causes a rapid equilibration of the system, resulting in a limited lifetime of the convection patterns. Hence, experimental systems with intermediate Ra values are required to establish solutal buoyancy convection patterns.

3.1 Self-organization emerging from reaction–convection systems in solution

Typically, generating the density gradient requires an interface. For example, Avnir *et al.* reported convection patterns in Petri dishes with solutions of pH indicators methyl orange or phenolphthalein.[95,97] Upon subjecting these solutions at the air–water interface to an ammonia vapour, which increases the pH in the top of the solution, the solution becomes denser in the top, and convection patterns form with concentric rings and mosaic structures. These observations also exemplify that studying reaction–convection patterns is most convenient when either the reactants or products are coloured. Additionally, convection patterns were shown to emerge from density-based instabilities in chemical waves generated by the chlorite–thiosulfate reaction,[98] whereas in the iodate arsenic acid reaction[99] and the iron(II)–nitric acid reaction,[100] density gradients are generated that add a convective component to the progression of reaction–diffusion fronts through solution. Furthermore, convection patterns emerge when hydrodynamic, typically density-related, instabilities are generated at the horizontal interface of two phases with reagents that are enclosed in a Hele-Shaw cell, for example through an acid–base reaction[101,102] or the dissolution of CO_2 from the gas phase into a NaOH solution.[103]

Experiments in our lab with the pH indicator bromothymol blue showed similar convection patterns (Fig. 8). We have activated a photoacid generator to decrease the pH in the top layer of the solution upon exposure to UV. Starting from pH $\approx$ 8, the acidification resulted in a change of the pH indicator bromothymol blue from green to yellow. Convection patterns

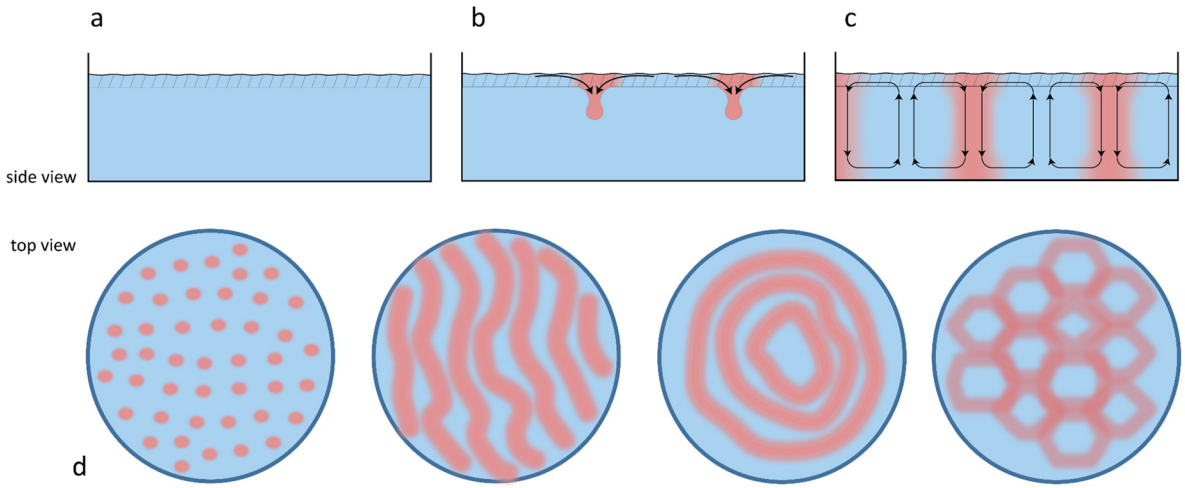

Fig. 7 The emergence of solutal buoyancy convection patterns driven by a chemical reaction. (a) Initially, the solution is homogeneous. (b) A high density reaction product (in red) is formed in the top layer of the solution, and descends to the bottom of the reaction chamber. (c) To balance the descending fluid flow, regions of ascending fluid flow appear. (d) Overall, convection cells appear, forming patterns that span the whole reaction chamber and depend on the geometry and liquid depth.

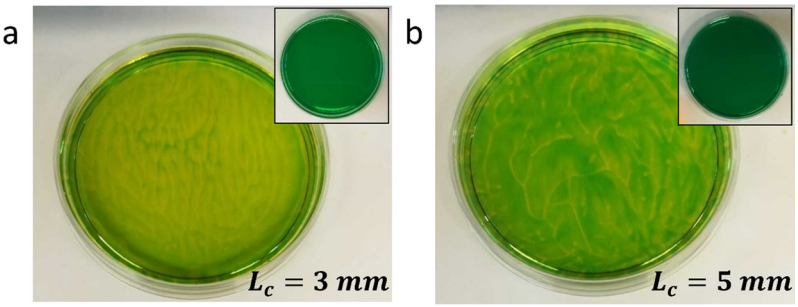

Fig. 8 Solutal buoyancy convection patterns in aqueous solutions of the pH indicator bromothymol blue (BTB). Upon slowly decreasing the pH by UV activation of photoacid generator NPE sulfate, the color of BTB changes from green to yellow. Concomitantly, changes in density generate convection patterns. (a) For a liquid depth L_c = 3 mm, the predominant convection patterns are parallel stripes. (b) For L_c = 5 mm, the predominant convection patterns are curved and branched. These images were taken after 5 minutes of UV irradiation. Insets show the homogeneous solution before irradiation. For both experiments: [BTB] = 0.1 mM, [NPE sulfate] = 1.4 mM, and irradiation wavelength λ_{UV} = 254 nm. To slow down the convection and increase the lifetime of the patterns, we increased the viscosity in both experiments by adding 1.1 g mL^{-1} PEG-2000. Unpublished results by A.-D. C. Nguindjel.

emerged over the course of 5 to 10 minutes, varying in shape from stripes (Fig. 8a) to branches and dots (Fig. 8b). Intriguingly, we observed that the patterns can be varied by varying the depth of the solution, *i.e.* L_c.

Surprisingly, despite the abundance of chemical reactions that potentially give rise to density differences, the implementation of chemo-hydrodynamic effects in chemical systems as a design principle, rather than a phenomenon as such, is quite rare. However, recent theoretical studies emphasize the untapped potential of reaction–convection: self-generated convection can accelerate chemical reactions,[104] and enhance nonlinear kinetics such as chemical oscillations.[105]

To engineer self-organizing convection patterns in solution, careful design of the chemical reactions is important. Enzymatic reactions with a constant production rate – in order to generate a steady density gradient – can relatively easily be tuned *via* the enzyme concentration. Furthermore, it is relatively easy to spatially restrict the region of chemical activity by immobilizing the enzyme(s), *e.g.* at the top or at the bottom of a reaction container. For example, Zhang *et al.* use an enzymatic reaction network comprised of two enzymes, glucose oxidase (GOx) and horseradish peroxidase (HRP).[106] GOx utilizes atmospheric oxygen at the top of the reaction container to oxidize glucose into gluconic acid and hydrogen peroxide. Due to gluconic acid being ~0.2% more dense than glucose, a vertical density gradient emerges.[107] The patterns are visualized *via* hydrogen peroxide, a side product of the glucose oxidation. HRP uses hydrogen peroxide to oxidize 2,2′-azino-bis(3-ethylbenzothiazoline-6-sulfonic acid) (ABTS) into $ABTS^{\bullet+}$. This green product visualizes the solutal buoyancy convection patterns. The patterns that appear were demonstrated to depend strongly on the liquid depth and evolve over time into different configurations.

Apart from self-organization into convection cells of various geometrical shapes, solutal buoyancy convection can be tailored to self-organize flow patterns into so-called chemical pumps.[108–111] By immobilizing enzymes at fixed locations in a container, substrates and products can be 'pumped' over centimetre-long distances if the density differences between substrates and products are large enough. The pump velocity is governed by the substrate concentrations and the reaction rate. Intricate flow patterns can be designed by combining sequential enzymatic reactions. For example, Maiti *et al.* engineered a bifurcating flow pattern using three different enzymes: glucose oxidase (GOx), catalase (CAT) and acid phosphatase (AP).[110] These three enzymes were separately immobilized in pieces of agarose gel and spaced apart 6–7 mm in a triangular configuration inside a reaction container. GOx and CAT take part in a reaction cascade while AP catalyses a separate reaction:

$$\text{Cascade: } \begin{cases} \text{Glucose} + O_2 \overset{\text{GOx}}{\rightarrow} \text{Gluconic acid} + H_2O_2 \\ 2H_2O_2 \overset{\text{CAT}}{\rightarrow} 2H_2O + O_2 \end{cases}$$

$$\text{PNPP} \overset{\text{AP}}{\rightarrow} \text{PNP} + NaH_2PO_4$$

Here, PNPP stands for *p*-nitrophenylphosphate (hexahydrate) and PNP stands for *p*-nitrophenol. At all enzyme-loaded gels, a density gradient emerges, because (1) glucose is less dense than gluconic acid; (2) hydrogen peroxide is denser than water and oxygen, and (3) PNPP is denser than PNP. At the start of the experiment, PNPP is loaded onto the GOx gel and the reaction chamber is filled with a D-glucose solution. Due to the concomitant conversion of glucose in gluconic acid and the leaking of PNPP into the surrounding solution, solutal buoyancy convection sets in. This flow is directed away from the GOx/PNPP gel. Subsequently, due to the reactions that take place in the AP and CAT gels, the convective flows self-organize to form a bifurcating flow pattern with flow velocities in the μm s^{-1} range.

3.2 Reaction–convection systems to shape self-assembled structures

Aside from self-organizing convection patterns of molecularly dissolved compounds in solution, convection can be applied to direct the organization of self-assembled structures. Leira-Iglesias *et al.* provide a demonstration of solutal buoyancy to affect the macroscopic organization of a supramolecular polymer.[112] During the self-assembly of perylene diimide (PDI) based monomers, the

assemblies aligned due to solutal buoyancy convection, driven by a 0.2% density mismatch between the PDI monomer and the PDI assemblies in solution. Depending on whether or not the polymerization was initiated by seeding with a small amount of PDI assemblies, the resultant PDI polymers aligned inside a centimeter-sized patch of outward pointing lines, or in multiple millimeter-sized polygon-shaped patches. Furthermore, inorganic solid structures with complex morphologies can emerge from a combination of reaction–diffusion, convection and precipitation reactions, resulting in chemical gardens and biomorphs.[113,114] Finally, the concept of viscous fingering results in chemo-hydrodynamic structures at the interface of two liquids, when the low-viscosity fluid enters the more viscous fluid phase.[115,116] Whereas the emergence of these fingers does not require a chemical reaction as such, it is shown how the viscous fingering amongst a low- and high-viscosity interface with the respective reagents can shape the structures that are formed upon the deprotonation of a polymer,[117] the assembly of wormlike micelles,[118] or crystallization.[119]

4. Marangoni flow systems

Surface tension gradients are an attractive design principle to establish organization at gas–liquid or liquid–liquid interfaces in out-of-equilibrium systems, *via* a simple chemical reaction (*e.g.* A → B, or A + B → C).[120] When an imbalance in surface tension is present, a mass transfer, named the Marangoni effect, occurs from the region of low surface tension towards the region of high surface tension.[121] Two types of Marangoni effect are generally described: thermo-capillary Marangoni flows are obtained when inhomogeneous heating of an interface leads to local changes in surface tension, while soluto-capillary Marangoni flows are established by the inhomogeneous repartition of a single surfactant in the system, or multiple surface active compounds with distinct surface tension properties. Regardless of their origin, these gradients induce tangential shear stresses at the interface, which in turn generate flow once the shear stress overcomes the viscous stress.[122,123] This balance is represented as follows:

$$\tau_t = -\mu\frac{\partial u_t}{\partial n} = \frac{\mathrm{d}\gamma}{\mathrm{d}X}\cdot\nabla X_t \qquad (2)$$

where t and n are the tangential and normal vectors respective to the interface, τ_t represents the shear stress tangential to the interface, μ the dynamic viscosity, u_t the tangential velocity vector and γ the surface tension. X stands for temperature (T) in case of thermo-capillary effect, or surfactant concentration (C) when considering soluto-capillary effects. Finally, ∇X_t represents the temperature or concentration gradient along the interface (Fig. 9). The probability of surface tension-driven instabilities to give rise to a mass transfer at an interface is usually represented by the dimensionless Marangoni number $\mathrm{Ma_T}$ or $\mathrm{Ma_C}$ for respectively thermo and soluto-capillary effects, which displays the balance between the induced shear stress and diffusion, and are defined as:

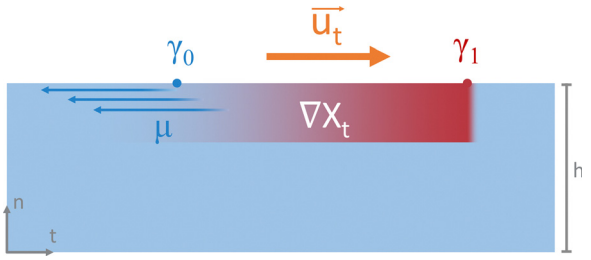

Fig. 9 Marangoni flow emerging from a surface tension gradient. The presence of a temperature or surfactant concentration gradient ∇X_t along a fluid interface translates into a surface tension (γ) gradient across the interface. The shear stress emerging from that event induces the mass transfer phenomenon known as the Marangoni effect. From there, liquids flow from the area of low surface tension (γ_0) towards the area of high surface tension (γ_1) with the velocity vector u_t that opposes the viscous stress.

$$\mathrm{Ma}_T = -\frac{\partial\gamma}{\partial T}\cdot\frac{h\Delta T}{\mu\alpha} \quad \mathrm{Ma}_C = \frac{\partial\gamma}{\partial C}\cdot\frac{h\Delta C}{\mu D} \qquad (3)$$

where h is the thickness of the film, α the thermal diffusivity, D the diffusion coefficient of the surfactant and ΔT or ΔC the temperature or concentration variation across the film. A positive Ma indicates the presence of instabilities in the system, which are only converted into flow when a critical Marangoni number is reached, matching with a critical ΔT or ΔC and therefore a critical $\Delta\gamma$. In such regime, the flow velocity is proportional to the surface tension gradient.

Marangoni flows are used in a wide variety of systems, and the examples selected here outline the diversity of approaches to create complex spatial organization. We focus on flows induced by the soluto-capillary effect, as – contrary to thermally-induced flows – they can be controlled by chemical reactions, and thereby offer a greater ability to program Marangoni flow in self-organizing systems.

4.1 Generating and sustaining surface tension gradients under non-equilibrium conditions

Surface tension gradients can be generated at 2D liquid–liquid or gas–liquid interfaces or in 3D systems at the interface of spherical droplets dispersed in solution.[124–126] In each configuration, the Marangoni flow displays characteristic range, velocities and duration that depend on the chemistry and the geometry of the system.

4.1.1 Surface tension gradients at 2D interfaces. Surface tensions gradients can be established by the release of surfactants at a specific location of a 2D interface. Typically, a surface active compound or low surface tension solvent is allowed to diffuse in solution from a source (*e.g.* a hydrogel loaded with surfactant solution), generating a flow away from the source. Camphor,[127–131] alcohol[132] and sodium oleate[133] have been successfully used as source compounds and demonstrated their efficiency to transport a variety of macroscopic objects (boats, tablets, *etc.*) over cm long distances. These systems allow for rapid motion of objects at the interface, however,

the lifetime of such flow is limited due to the rapid saturation of the interface (*i.e.* $\Delta C = 0$) or depletion of the source.

A supramolecular approach was used by Cheng *et al.* in their attempt to extend the lifetime of a Marangoni flow induced by a gradient of sodium dodecyl sulfate (SDS) at an air–water interface.[134] Similar to the boat experiments presented above, SDS is gradually released in solution from a hydrogel source, giving rise to a Marangoni flow sustained for approximatively 45 s, before the surface tension is evened out. The system is altered to prevent interfacial saturation with the introduction of cyclodextrin as a complexation agent in the medium. By sequestering the surfactant in a supramolecular complex that readily dissolves in the bulk solution, the system is sustained far from equilibrium. The simultaneous release and capture of SDS dramatically extends the time for which the Marangoni flow is sustained by a factor 50.

To further control the way the flow is established and the period for which it is sustained (and so for which $\Delta C > 0$), chemical reactions that impact the surface tension are particularly useful. Here, instead of relying on deposition, a gradient is established from an initially homogeneous interface by introducing reactions that locally produce or consume surface active compounds. The chemistry of fatty acid compounds is mainly used in such examples, because their acid/base properties are directly coupled with their surface activity. Indeed, the difference in surface tension between the protonated (high γ) *vs.* the deprotonated (low γ) forms of these compounds is significant enough to generate instabilities, meaning that the presence of a pH gradient can eventually lead to Marangoni flow. Lagzi *et al.*[135] and later Suzuno *et al.*[136] take advantage of the properties of 2-hexyldecanoic acid to solve mazes at a liquid-air interface. In both examples, a pH gradient is established in a solution containing the fatty acid by placing a hydrogel pre-soaked in concentrated acid at the exit of the maze. In that setting, protons diffuse away from the hydrogel source and the subsequent protonation of the fatty acid occurs unevenly at the interface, giving rise to a Marangoni flow that drags objects floating at velocities up to 10 mm s^{-1} directly towards the maze exit within seconds.

In a work recently published by our research group, the need for an external source of protons is eliminated upon using a photochemical reaction.[137] Starting from a homogeneous aqueous solution containing a photoacid generator and the surface active sodium oleate, a pH gradient is established upon local irradiation of the interface (Fig. 10a). The rapid acidification of the medium leads to the protonation of oleate into oleic acid. Apart from displaying a higher surface tension than its deprotonated counterpart, oleic acid tends to phase-separate into oil droplets, which enhances the gradient. We have demonstrated that the Marangoni flow, by continuously bringing unreacted photoacid and oleate towards the irradiated area could sustain itself over extended periods of time of up to 30 minutes. Moreover, careful investigation into the ratio of sodium oleate over photoacid introduced in the system demonstrated that the flow velocity and duration could be accurately controlled.

Considerable advantages of chemistry-induced gradients can be anticipated with the way chemical reactions can be coupled with one another into networks. The reversibility of acid/base chemistry can also be an asset in efforts to increase the complexity of the system and possibly generating feedback loops.

Over the past decade, photoswitches have gained traction for their ability to remotely modify surface properties, because of

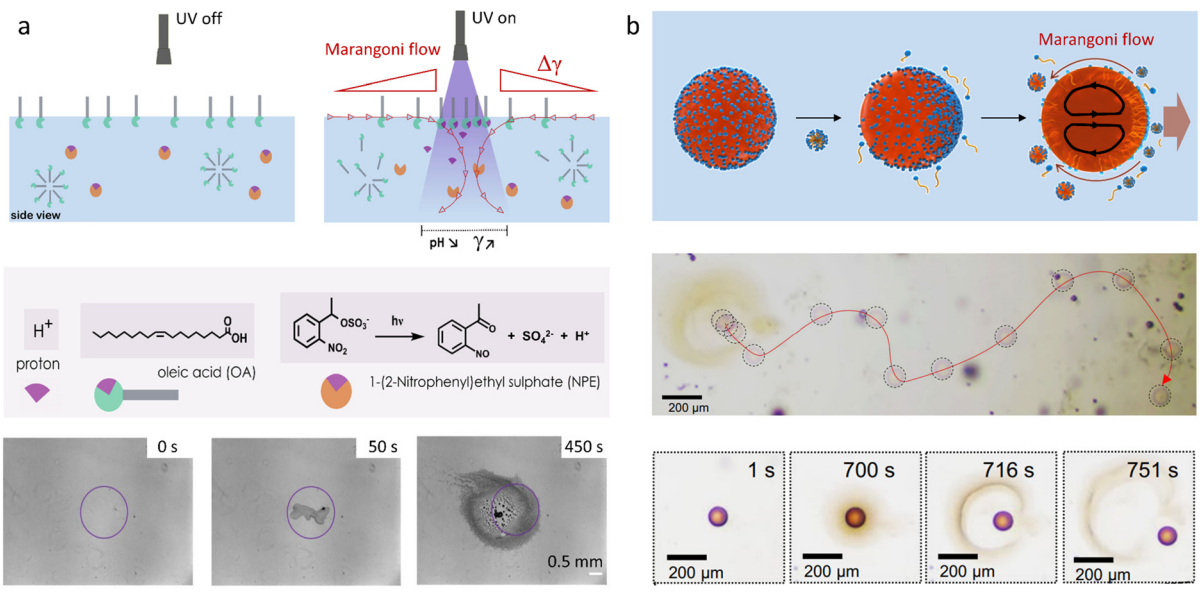

Fig. 10 (a) Self-sustained Marangoni flow at a 2D air–water interface, triggered by local UV exposure. Photoacid generator 1-(2-nitrophenyl)ethyl sulfate (NPE sulfate) produces an acid, which protonates the surfactant oleate. Thereby, the surface tension increases at the site of UV exposure, where phase separated oleic acid droplets accumulate. Adapted from ref. 137 with permission from the Wiley-VCH publishing group, Copyright 2021. (b) Propulsion of octanol droplets in an aqueous solution (*i.e.* 3D system): an asymmetric occupation of lipid (of which the formation is catalyzed by the octanol-water interface) at the droplet interface results into an internal Marangoni flow in the droplet, which drives their propulsion. Adapted from ref. 147.

their light sensitivity and their high reversibility.[138,139] In a variety of studies, amphiphilic molecules containing a photoswitchable azobenzene moiety have been synthetized to control interfacial mass transfer. These systems, exemplified by the work of Diguet *et al.*, rely on the drastic change in surface activity displayed by the *trans* (low γ) and *cis* (high γ) isomers (in some cases +10 mN m^{-1})[140] to generate stimuli-responsive Marangoni flows.[141] In a work by Lv *et al.*, the trajectory of polystyrene microparticles present at an air–water interface is manipulated by using such a photoswitch.[142] Upon light activation (laser irradiation at 442 nm) of an interface covered with the *trans* surfactant, local *cis* isomerisation leads to the transport and trapping of the particles at the beam location. The use of multiple laser beams in close proximity reveals the possibility to manipulate adjacent surface tension gradients to control the positioning of multiple particles.

4.1.2 Surface tension gradients in 3D systems. Three-dimensional Marangoni flows are generally obtained by breaking the interfacial symmetry of spherical droplets immersed in liquid environments. While some of the approaches used in 2D systems can be adapted, others are unique to the geometry of these interfaces. Schmitt and Stark demonstrate how liquid droplets immersed in surfactant solutions can display spontaneous self-propulsion from an initially homogeneous environment.[143] They explore the emergence of Marangoni flow at a droplet interface when the interfacial symmetry is broken by the local adsorption of micelles, which occurs at sufficiently large Péclet number (strong advection, weak diffusion). In this scenario, the droplet interfacial tension is reduced at the site where the micelle is adsorbed, inducing a mass transfer along the interface from the adsorption front to the rear of the droplet. The resulting persistent self-propulsed motion is explained by the internal flow that pushes the droplet in the direction of the adsorption site and generates an external flow field. The trajectory and speed of a typical droplet, along with the internal and external flow fields, can be simulated as a function of the adsorption rate, highlighting one of the key parameters regulating the flow in such systems. Furthermore, photoswitchable surfactants – applied in 2D interfaces as well – can be applied to break the interfacial symmetry. For example, the *trans–cis* isomerization of azobenzene-based surfactants can result in droplet propulsion towards or away from the laser beam. Less commonly, spiropyran photoswitches can be used to manipulate the interfacial tension by switching the compound between its closed spiropyran (low γ) and open merocyanin (high γ) forms using UV/blue light. Recently, Xiao *et al.* controlled the 3D motion of an aqueous droplet immersed in oil *via* this photoisomerization, as the internal Marangoni flow can be induced in any direction by simply modifying the orientation of the light source.[144] This example highlights the strategic advantages in gaining control of the spatial organization of surface/interfacial gradients in chemical systems.

Self-propulsion of droplets immersed in a micellar continuous phase can also occur when the micelles present in the system are able to partially solubilize the droplet phase. This phenomenon is exemplified by Izri *et al.* where water droplets are immersed in solutions of squalane and monoolein.[145] Monoolein, which acts as a surfactant, ensures the stability of the emulsion by covering the droplets interface. When its concentration exceeds the critical micelle concentration (CMC), surfactant molecules present at the water-squalane interface migrate to the bulk to join the newly formed micelles, which in turn begin to solubilize water in the squalene running phase, thereby displaying the above mentioned symmetry breaking. A surface tension gradient emerges at the droplets interface because they are no longer homogeneously covered with surfactant, and self-propulsed motion is observed with velocities ranging between 10 and 50 μm s^{-1}.

In a similar system, Thutupalli *et al.* demonstrate that chemical reactions involving monoolein at water droplets interface can be at the origin of self-propulsion and collective behaviour.[146] The aqueous droplets, immersed in squalane and monoolein, contain bromine, or reagents leading to bromine formation. At the droplet interface, bromine readily reacts with the monoolein double bond, to form a less active brominated surfactant. The subsequent surface tension imbalance results in active droplets, of which the internal and external velocity fields can be computed by taking into account the relation between surface tension and the bromination density. Collective behaviour, signified here by the polar alignment of the velocities of neighbouring droplets, is observed experimentally and explored theoretically, revealing that the interaction of self-propulsed droplets in a high density environment may lead to the formation of ordered structures.

In a work performed by Babu *et al.*, another type of chemical system is used to trigger the motion of organic droplets.[147,148] The authors show that the lipid-forming reaction between 1-hexanethiol and 2-methacryloyloxyethyl phosphorylcholine can be exploited to induce the propulsion of octanol droplets immersed in an aqueous medium (Fig. 10b). The lipid formation is catalysed by the octanol–water interface, leading to a homogeneous lipid coverage of the octanol droplets. Over time, the lipid concentration increases in the medium and they begin to self-assemble into micelles that partially solubilize the octanol in water. The recruitment of lipids into micelles results in a non-homogeneous coverage of the droplets and thus in symmetry breaking which leads to internal Marangoni flow. This work demonstrates that for a specific droplet/surfactant couple, a critical propulsion concentration, beyond the CMC value, needs to be reached to observe motion in the system.

Lastly, a recent study by Cheon *et al.* demonstrates that the self-propulsion of oil droplets in micellar solutions can be drastically enhanced by the addition of silica particles.[149] They hypothesize that the adsorption of these particles at the rear of the droplet interface helps to further polarize the droplet and thereby enhance the Marangoni induced-propulsion. While the precise mechanism is not clarified yet, this effect is observed for a wide range of surfactants and oil and so, opens new perspective in the domain of self-propelled droplets.

4.2 Examples of self-organized systems using surface tension gradients

When it comes to the Marangoni effect, self-organization seems particularly likely to emerge in systems relying on a two-body

interaction or the collective behaviour of multiple objects placed at a fluid interface. Even though such 'two-body' systems all depend on the difference in surface property of two distinct objects, they encompass a wide variety of complex interactions to drive the self-organization.

In a source-sink configuration, the surface tension gradient is sustained by the interaction between an object that generates a Marangoni flow (source) and another one that absorbs surface active compounds (sink). Our research group has used such dynamics to obtain self-organized patterns between source and drain droplets deposited at an 2D air–water interface.[150] Here, source droplets composed of the surfactant tetraethyleneglycol monododecyl ether ($C_{12}E_4$) are used not only to generate a surface tension gradient by releasing the surfactant, but also for their ability to grow centimetre-long, multi-lamellar wire-like structures called myelin figures. We showed that to form patterns, the positioning of these sources can be mediated by the presence of liquid organic droplets that act as sinks by absorbing $C_{12}E_4$ from the air–water interface (Fig. 11a). The resulting Marangoni flow accelerates the growth of the myelin figures from the source droplet, while simultaneously directing them towards the sink droplets. Upon adsorption at the sink, the myelin figures impose a force on the sink droplet, drawing it towards the source until the attractive force is balanced with the repelling Marangoni flow (Fig. 11b and c).[151] Along with a kinetic model, we demonstrated experimentally that the composition of the sink determines its capacity for surfactant uptake, and thereby on the self-organization of the myelins-droplet networks.

A different type of source-sink configuration is developed by Meredith *et al.* where organic droplets immersed in an aqueous Triton X-100 micellar solution display predator-prey behaviour (Fig. 12a).[152] In this 3D system, the difference in micellar solubilisation rate between droplets of 1-bromooctane (BOct) and ethoxynonafluorobutane (EFB), respectively used as source and sink, is exploited to give rise to complex chase dynamics. In a first step, the BOct predator droplets deplete their surroundings from Triton X-100 by recruiting the surfactant to form BOct-filled micelles (Fig. 12b). This produces a gradient of filled micelles that tends to repel other predator droplets, as the depletion of surfactant generates an asymmetric surfactant occupation at the droplet interface, which drives its motion away from the other BOct droplet. On the contrary, EFB prey droplets are able to have non-reciprocal interactions with their predators because they are resistant to micellar solubilisation and thus induce no repulsion. When EFB preys are in proximity to their BOct predators, they primarily interact with the filled micelle gradient by taking up the BOct that they carry, emptying

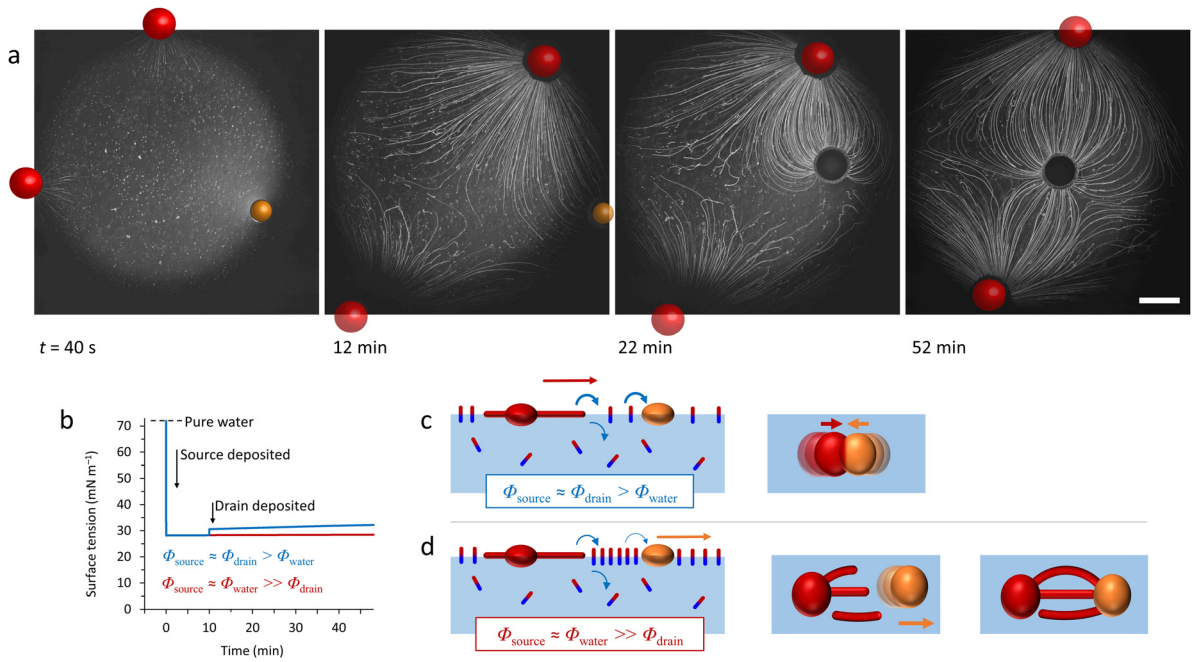

Fig. 11 Self-organized source-sink system driven by Marangoni flows. (a) Optical microscopy recordings of an air–water interface where a newly deposited oleic acid sink droplet (orange) positions itself between two $C_{12}E_4$ source droplets (red). The interaction between the three floating droplets is mediated by the attractive and repulsive forces originating from the local surface tension gradients at the interface. The source droplets grow myelins and release surfactant molecules in solution, inducing a surface tension gradient. The repelling Marangoni flow that they generate is balanced by the sink droplet that absorbs the surfactant and tethers to the myelins, leading to self-organization into a linear pattern. The scale bar is 2 mm. (b) Simulation of the dynamic surface tension based on $C_{12}E_4$ release rate from the source (Φ_{source}), its absorption rate by the sink (Φ_{drain}) and its desorption from the interface (Φ_{water}). The blue curve represents a situation where the deposition of the sink induces a local surface tension gradient because it absorbs the surfactant faster than it desorbs from the interface. In opposition, the red curve shows a situation where the desorption is faster than the absorption. (c) The schemes present the impact of the dynamic surface tension on the droplets' positioning. The top, absorption-dominant situation leads to attraction between source and sink. The bottom, desorption-dominant situation leads to repulsion of the sink away from the source, followed by tethering of the myelins to the sink, which keeps the sink in position. Adapted from ref. 150.

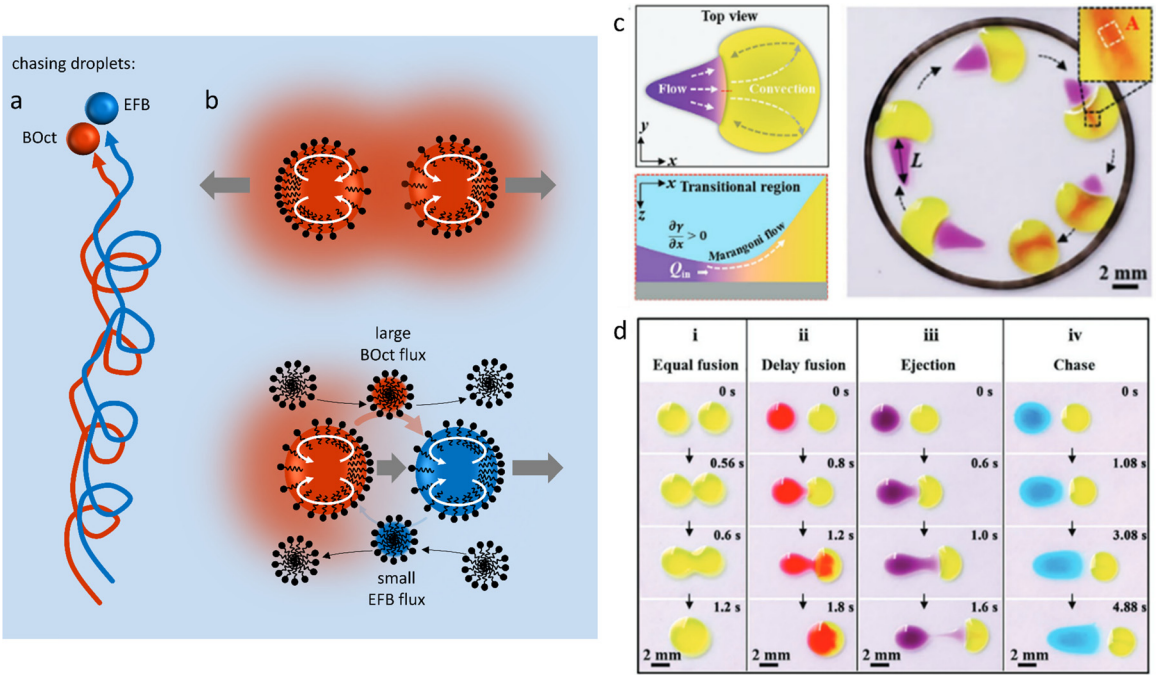

Fig. 12 Self-organized motion in two-body systems. (a) Chase dynamics between BOct (red) and EFB (blue) droplets immersed in a micellar Triton X-100 solution. The BOct predator droplet chases after the EFB prey droplet. Once the predator has caught the prey they keep moving as a pair in the solution. (b) The scheme details the non-reciprocal mechanism behind the chase: (1) BOct is solubilized in the Triton micelles, creating a repelling gradient of filled micelles around it (top scheme). (2) BOct-filled micelles diffuse in the solution and the transported oil is taken up by the EFB droplets, releasing new free micelles at the back of the prey. (3) The free micelles are adsorbed at the front of the predator droplets, triggering the Marangoni propulsion of the predator towards the prey (bottom scheme). (4) The preys also escape the predator by using Marangoni propulsion, moving towards areas rich in empty micelles.[152] (c) Self-driven droplet vehicle actuated by the Marangoni effect. The vehicle is made of two droplets (head in yellow, tail in purple) adsorbed on a solid substrate. The surface tension difference between head (high γ) and tail (low γ) generates a convective flow that enables the vehicle to move into a confined space until the tail merges with the head. (d) Table recapitulating the type of vehicle interaction (fusion, delay fusion, ejection, chase) that can be obtained when the surface tension of the tail droplet is decreased while the head droplet is kept constant. (c and d) Reproduced from ref. 154 with permission from the Wiley-VCH publishing group, Copyright 2021.

the previously filled micelles. The adsorption of these newly-formed empty micelles at the front of BOct droplets triggers the internal Marangoni propulsion that is at the origin of the chase, as the prey droplet flees from the predator towards regions with an even lower concentration of solubilized oil. This dynamic behaviour is sustained by the gradient in BOct-filled micelles and can therefore be modulated by the Triton X-100 concentration in the aqueous phase. Increasing the density of predators and prey in a system also leads to self-assembled clusters displaying remarkably complex interactions based on the same non-reciprocal exchanges.

Self-driven droplet vehicles developed by Cira *et al.*,[153] and further explored by Li *et al.*[154] are fascinating examples of the versatility present in two-body systems. These vehicles consist of two liquid droplets with distinct surface tensions at their air–liquid interface, that are deposited on a solid substrate, one serving as head and the other as tail (Fig. 12c). When in contact, the convective flow that is generated because of the surface tension difference between the two liquids constitutes the driving force of the vehicles (Fig. 12d), and Li *et al.*[154] demonstrate that this surface tension difference must exceed 5 mN m^{-1} while the size ratio of the droplets (D_{head}/D_{tail}) must be above 1.6 to display propulsion. Interestingly, they revealed that increasing $\Delta\gamma$ did not systematically induce an increase in propulsion velocity and that the latter was in fact determined by the surface tension coefficient $\bar{\gamma}/\Delta\gamma$, where $\bar{\gamma}$ represents the average of the initial γ_{head} and γ_{tail}, and $\Delta\gamma$ is the difference between the initial γ_{head} and γ_{tail}. Finally, they show that by carefully choosing the liquids, the vehicles can efficiently deposit colloidal particles at solid surfaces into patterns at the microscale.

In a work published by Liu *et al.*, decanol droplets are driven through complex pathways at a liquid interface by surface tension gradients induced with organic solvent vapours.[155] The decanol droplets are deposited on aqueous ethanol solutions while carbon tetrachloride (CCl_4) vapour is released from droplets suspended on a glass substrate placed a few millimetres above the interface (Fig. 13a). The CCl_4 vapour locally increases the surface tension and therefore generates Marangoni flows that attract the decanol droplets, towards the vapour-rich area. Intriguingly, the use of multiple droplets at the interface reveals the possibility to generate dynamic droplet patterns. Here, CCl_4 is placed on the glass substrate to form the letter T, H or U, and when placed over the interface, the decanol droplets organize according to that shape while maintaining a distance between one another. This out-of-equilibrium process is controlled by the attractive Marangoni flow, driven by the

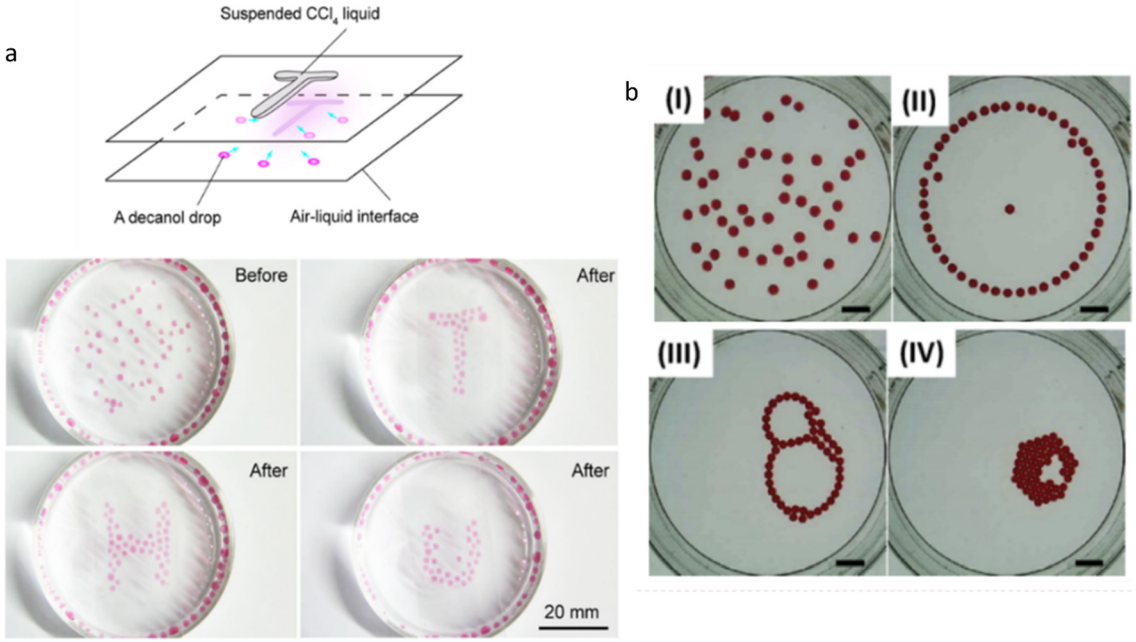

Fig. 13 Collective behaviour in multi-droplets systems. (a) Decanol droplets at air–water interface self-organize into various letter-shaped patterns under the influence of CCl_4 vapours. The latter are used to increase the local surface tension of the interface and subsequently attract the decanol droplets. The patterns are then sustained by the simultaneous action of the Marangoni effect and the repulsion exerted by each droplet. Reprinted (adapted) with permission from ref. 155. Copyright 2019 American Chemical Society. (b) Dynamic self-organized patterns are observed when ethyl salicylate droplets are deposited over an aqueous SDS solution. The initially random arrangement (I) evolves to successively form a ring (II), a chain-like structure (III) and eventually a compact cluster (IV). The organic droplets partially solubilize in the surfactant-rich medium over time, each generating its own Marangoni flow. The transformation of the patterns is therefore understood to be the result of the complex interaction between the local surface tension gradients produced by each individual droplet, and capillary interaction. The scale bar is 10 mm. Reprinted from Colloids and Surfaces A, 566, J. Čejková, K. Schwarzenberger, K. Eckert, S. Tanaka, Dancing performance of organic droplets in aqueous surfactant solutions, 141–147, Copyright 2019, with permission from Elsevier.

CCl_4 vapour, and the repulsive interaction between the decanol droplets, which is driven by the outward Marangoni flow when the droplets are in close contact. Together, this shows promise for the emergence of collective effects in multi-droplets systems.

In experiments involving TiO_2 particles at a silicon oil–water interface, Wittmann *et al.* observed Marangoni-induced collective motion upon UV irradiation of the system.[156] The particles are adsorbed onto the interface because of the presence of the surfactant Triton X and they catalyse the photo-degradation of H_2O_2 in the aqueous solution. They report that the spherical particles, which individually display no motility due to their symmetry, are able to collectively move towards an area exposed to UV when they are present as a monolayer, indicating that a collective effect is at the origin of the phenomenon. Throughout their investigation, they rule out possible thermal or phoretic effects and argue that the inhomogeneous repartitioning of the particles at the oil–water interface along with the interface response to the photochemical activity is responsible for symmetry-breaking events leading to a Marangoni flow. The system appears to be maintained in an out-of-equilibrium state by continuous UV exposure, and therefore continuous H_2O_2 decomposition, as the particles' motion is interrupted as soon as the irradiation is stopped. Additionally, they demonstrate the existence of a particle density dependence on flow behaviours. In low density settings, the TiO_2 particles gather in the irradiated area within seconds and then immediately bounce away from it while in high density settings, they gather and accumulate in the irradiated area to form a stable cluster.

Intriguing collective effects are observed by Tanaka *et al.*, and further explored by Čejková *et al.* when droplets of decanol or ethyl salicylate (ES) are respectively deposited at the interface of sodium decanoate or SDS aqueous solutions.[157,158] The organic droplets first display individual random motion, but then evolve into self-organized dynamic clusters. Three consecutive cluster configurations are showcased in both systems (Fig. 13b). First, a geometrical configuration is obtained where the droplets arrange themselves into a semi-static pattern, circular for ES droplets and squared for the decanol droplets. Over time, these patterns become less stable and eventually collapse, followed by the emergence of a second configuration. Here, the cluster appears to be oscillating because droplets form chain-like structures where they continuously permutate with one another. In the third configuration, the droplets merge *via* capillary attraction into compact clusters that remain static for hours. The complex interaction between each droplet and the surfactant solution seems to be at the origin of the unique configurations displayed in both systems. Indeed, a study of the decanol droplets in decanoate solution reveals that partial dissolution of the droplets in the medium decreases the local surface tension and thus generates a Marangoni flow away

from them. In this context, it is hypothesized that the varying intensity of the Marangoni flow generated from each droplet mediates the interaction, repulsive or attractive, between the members of the cluster.

5. Diffusiophoresis systems

Diffusiophoresis is well-established as a mechanism to drive the directional motion of objects, such as colloidal particles, up or down concentration gradients in solution, with speeds that are impossible to establish with Brownian motion (up to 1–10 μm s^{-1}).[159] This opens perspectives to direct self-organization. The motion of a particle up or down a solute concentration gradient is driven by the favourable or unfavourable interaction between solute and particle. In electrolyte-based (ionic) gradients, diffusiophoresis typically generates faster particle velocities compared to non-electrolyte gradients.[159] Furthermore, self-diffusiophoresis, where particles migrate along self-generated gradients, typically involves electrolytes.[160] In many self-organizing systems where electrolyte gradients induce the motility of charged colloidal particles, the velocity of the particles is dominated by the electric field that spontaneously emerges in a concentration gradient of ions with different diffusion coefficients. For example, for an ammonia solution, $D(NH_4^+) = 1.96 \times 10^{-9}$ m^2 s^{-1}, and $D(OH^-) = 5.27 \times 10^{-9}$ m^2 s^{-1}, and therefore, OH^- diffuses faster down the ammonia concentration gradient that is released from the spherical source in Fig. 14a. Thereby, an electric field arises that concomitantly slows down OH^- diffusion and speeds up NH_4^+, in order to enhance local electro-neutrality in the solution. This electric field $E = \frac{k_B T}{Ze}\beta\frac{\nabla c}{c}$ drives charged particles, with zeta potential ζ_p, with a speed $U = \frac{\varepsilon\zeta_p E}{\eta}$ down the electric field. Here, β represents the diffusivity difference factor: for symmetric Z:Z electrolytes (*i.e.*, equally charged cations and anions), $\beta = (D_+ - D_-)/(D_+ + D_-)$, where D_+ and D_- represent cation and anion diffusivity, respectively. ε is the dielectric permittivity of the medium, η the viscosity of the medium, and $\nabla c/c$ the relative concentration gradient of the electrolyte (in m^{-1}). This relationship implies that an ammonia gradient decreasing along the x-axis ($dc/dx < 0$) causes a negatively charged particle ($\zeta_p < 0$) to move up the concentration gradient ($U < 0$), since $\beta < 0$ for NH_4^+/OH^-, and a positively charged particle to move down the gradient. *Vice versa*, upon release of an electrolyte with a cation diffusing faster than the anion ($\beta > 0$), a positive particle will move up the concentration gradient, and a negatively charged particle will move down the gradient (Fig. 14b). Alternatively, if an electrolyte gradient with unequal diffusion constants of cat- and anions is established along a charged substrate, the counter ions of this substrate will be exposed to the electric field that is generated by the differential ion diffusion. As a result, an electroosmotic flow emerges along the substrate, as schematically shown in Fig. 14c.

5.1 Self-organization by electrolyte diffusiophoresis

Electrolyte diffusiophoresis has been demonstrated to drive the motion of a wide variety of charged particles along electrolyte gradients, where the path of the particles is determined by the concentration profile.[161] For example, Squires *et al.* have demonstrated how hydrogels that slowly release electrolytes serve as beacons that attract or repel charged colloidal microparticles over distances as long as 1 mm.[162] In pH gradients that are sustained by complementary hydrogel couples that release base and acid, respectively, 1 μm-sized negative polystyrene particles were transferred at speeds larger than 2 μm s^{-1} over a distance of approx. 1 mm from the acid to the base source, resulting into emerging flow patterns as shown in Fig. 15a. These observations highlight the strong contribution of OH^- and H^+ to the electric fields that are generated, since both OH^- ($D = 5.27 \times 10^{-9}$ m^2 s^{-1}) and H^+ ($D = 9.31 \times 10^{-9}$ m^2 s^{-1}) diffuse significantly faster than their respective counter-ions (typically $D \approx 1 \times 10^{-9}$ m^2 s^{-1}). Additionally, the acid-base reaction sustains the diffusion of acid and base from the respective sources.

Furthermore, McDermott *et al.*[163] reported self-generated flow patterns that emerge from calcium carbonate micropumps,

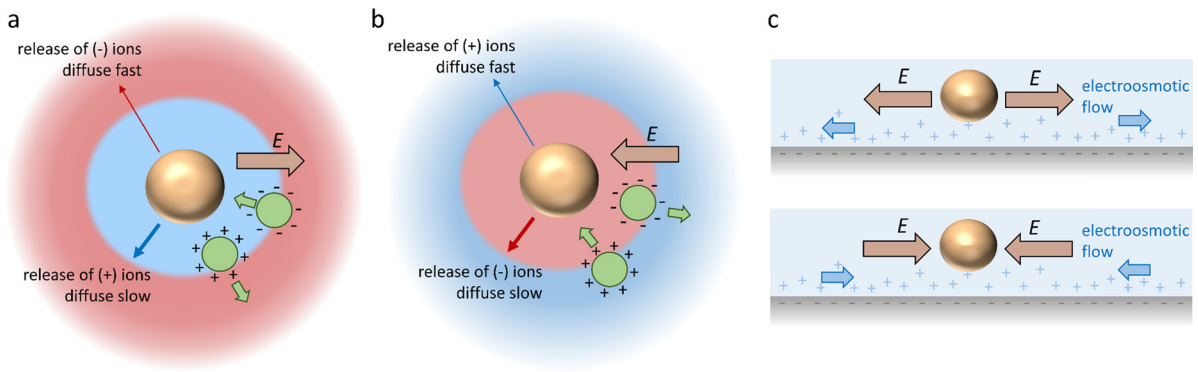

Fig. 14 Directional motion *via* electrolyte diffusiophoresis. (a) When the source (orange sphere) releases an electrolyte with $D_- > D_+$ (*i.e.* anion diffuses faster than cation), an electric field E emerges that attracts negatively charged particles (green sphere) towards the source, and repels positively charged particles. (b) *Vice versa*, with $D_+ > D_-$, the electric field attracts positively charged particles and repels negatively charged particles. (c) When the electrolyte gradient is established along a charged substrate, the effect of the electric field on the counter ions generates an electroosmotic flow away from (top) or towards (bottom) the electrolyte source.

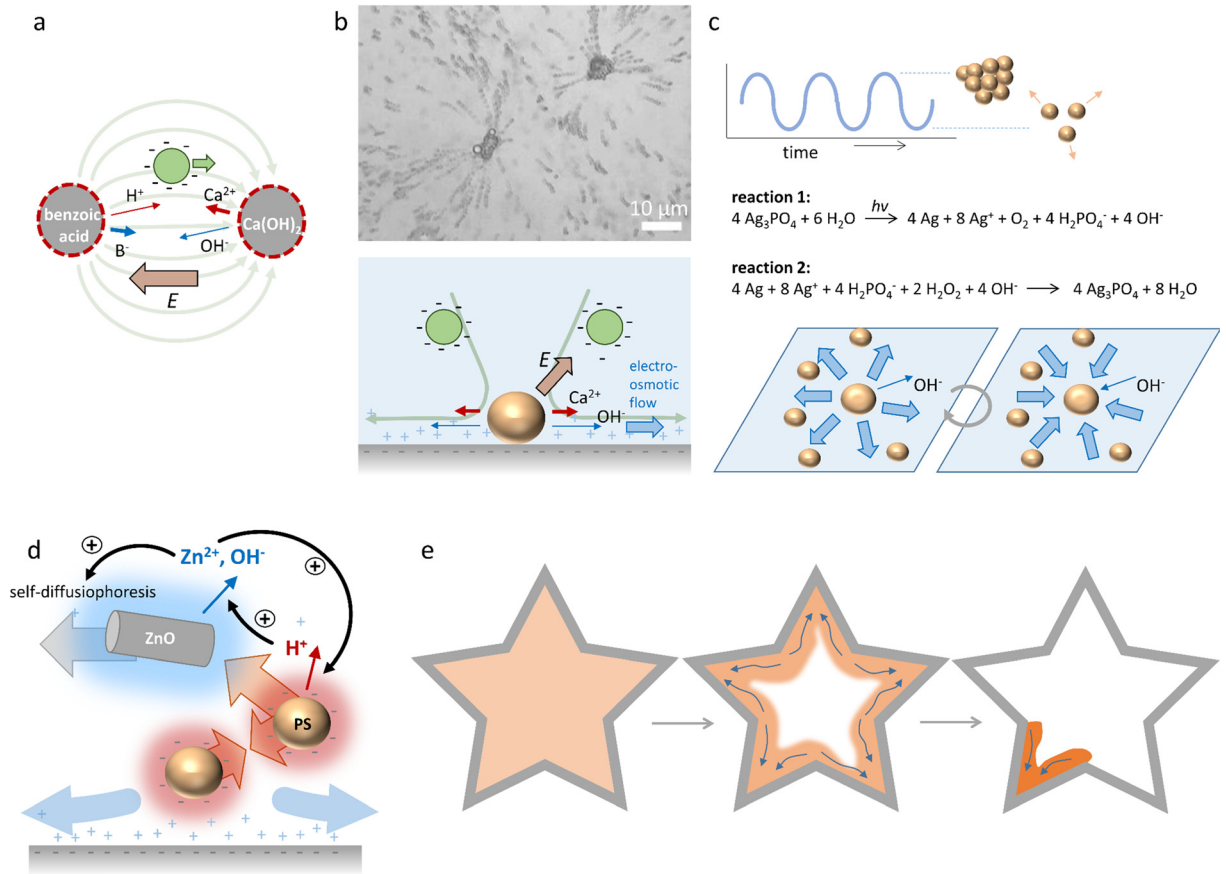

Fig. 15 Self-organisation driven by diffusiophoresis. (a) Motion pattern of negatively charged tracer particles along a sustained pH gradient between benzoic acid and $Ca(OH)_2$ sources.[162] (b) Electroosmotic flow drives the motion of tracer particles amongst $CaCO_3$ microparticles on a negatively charged substrate. Reprinted (adapted) with permission from ref. 163. Copyright 2012 American Chemical Society. (c) Oscillatory clustering and dispersion of Ag_3PO_4 microparticles in an aqueous H_2O_2 solution, where reaction (1) and (2) alternate and drive the electroosmotic flow.[170] (d) Diffusiophoretic colloidal swarms based on ZnO nanorods and sulfonated polystyrene microbeads, that are coupled *via* an ion exchange reaction that provide positive and negative feedback to ZnO/polystyrene clustering. (e) Collective swarm behaviour of ZnO/polystyrene particles (orange) that accumulate in the edge of the geometry (grey) with the highest curvature.[171]

where $CaCO_3$ microparticles slowly dissolve and generate an ionic gradient of Ca^{2+}, HCO_3^- and OH^- ions in the surrounding solution. Due to the high diffusion constant of OH^-, an electric field of 1–10 V cm^{-1} is generated, which is oriented away from the $CaCO_3$ microparticles. This electric field attracts negatively charged sulfate-functionalized polystyrene tracer particles towards the $CaCO_3$ microparticles. Interestingly, as the tracer particles approach the surface underneath the $CaCO_3$ microparticles, they are rapidly ejected radially outward in solution, as shown in Fig. 15b. The flow pattern of the tracer particles exemplifies the electroosmotic flow, which originates from the electric field that is generated around the dissolving $CaCO_3$ microparticles, and exerts its influence on the counterions of the negatively charged substrate.

In addition to particles that move in external concentration gradients, self-organization of dynamic colloidal swarms can emerge from a homogeneous dispersion of particles *via* autophoresis.[160] Here, the colloids self-generate a gradient of ions, which provides the electric field that is required for their propulsion and leads to organized collective behaviour. This concept has been exploited in self-assembly,[164,165] dynamic clustering,[166] schooling[167,168] and predator-prey behaviour of colloidal systems.[169] Recently, it has been shown that autophoretic systems can be classified as being either self-diffusiophoretic, when a net ion production occurs, or self-electrophoretic, when the net ion production is zero (*i.e.*, ions are released at one side of the particle, and consumed at the other side).[160] Self-diffusiophoretic colloids tend to move slower in a denser population, and form clusters that grow over time, whereas the motility of self-electrophoretic colloid clusters is independent of their density, and results in dynamic clusters with limited sizes.[160]

Collective, oscillatory behaviour of colloidal swarms has been reported by Altemose *et al.*[170] Silver orthophosphate microparticles (Ag_3PO_4) are dispersed in an aqueous hydrogen peroxide (H_2O_2) solution that is exposed to continuous UV illumination. Two opposing reactions occur: (1) reduction of silver ions (Ag^+) to silver metal (Ag) under UV illumination, and (2) oxidation of Ag to Ag^+ by H_2O_2 (Fig. 15c). As OH^-, which is formed upon the photo-reduction, has a higher diffusion coefficient than the positive ions that are produced, an electric field is generated which is directed away from the Ag_3PO_4

microparticles. This electric field acts on the positive counterions of the underlying glass substrate, resulting in an electroosmotic flow away from individual Ag_3PO_4 microparticles, which drives their mutual repulsion in the swarm. However, the re-oxidation (reaction (2)) consumes OH^-, and thereby reverses the electroosmotic flow. This causes the Ag_3PO_4 microparticles to attract each other and form compacted clusters. At the onset of the experiment, microparticles form stable clusters in the presence of H_2O_2 and UV, and after approx. 5–10 min, instabilities emerge that cause the clusters to disperse. Subsequently, the combination of both reactions causes the microparticles to periodically cluster and disperse. Intriguingly, these oscillations can be synchronized among neighbouring clusters through the diffusion of ions, and oscillation frequencies can be controlled *via* the H_2O_2 concentration.

Recently, Wu *et al.*[171] reported diffusiophoretic colloidal swarms inspired by a microbial symbiosis system, where the waste product of one chemical species is the nutrient that drives the motility of the other, and *vice versa* (Fig. 15d). To this end, ZnO nanorods and sulfonated polystyrene microbeads are coupled *via* an ion exchange reaction. ZnO nanorods release Zn^{2+} and OH^- in solution, resulting in self-diffusiophoresis that propels the nanorods with velocities up to 2 μm s^{-1}. As the polystyrene microbeads are negatively charged, they are attracted *via* electrophoresis along the Zn^{2+} gradient towards the ZnO nanorods. At the same time, the porous polystyrene microbeads take up Zn^{2+} and release H^+ *via* an ion exchange reaction. The H^+ gradient that is generated around the negatively charged PS beads causes them to attract each other *via* an electroosmotic flow at the substrate. Furthermore, the high H^+ concentration around the PS bead clusters lowers the local pH, which enhances Zn^{2+} release as the polystyrene beads approach the ZnO nanorods. Together, the ion exchange between ZnO nanorods and polystyrene microbeads generates a positive feedback that enhances the motility of both. However, close to the glass substrate, underneath the ZnO nanorods/polystyrene microbeads conglomerates, an outward electroosmotic flow is generated, which disassembles the aggregates. Together, the dynamic coupling of the ZnO nanorod/polystyrene microbead system through interconnected ion-exchange reactions allows for hierarchical and dynamic swarm behaviour (Fig. 15e). The clustering of the aggregates is enhanced when high concentrations of Zn^{2+} and H^+ accumulate at the edge of the sample chamber. As a result, the ZnO and polystyrene particles accumulate at all edges and corners present in the geometry of the system. Over the course of the accumulation, the highest curvature confines the ions most successfully. Once a threshold accumulation is reached, the mixture acts as a collective swarm and all colloids migrate towards the sharpest corner – in analogy to the quorum sensing routines displayed by microorganisms.

6. Outlook

The examples of self-organization highlight the potential of reaction–diffusion coupling, reaction–convection, the Marangoni effect and diffusiophoresis to sustain physicochemical gradients, which are critical to shape concentration patterns in solution, drive the self-assembly of out-of-equilibrium structures, or direct the organization of colloidal swarms. Importantly, the emergence of a stable gradient, rather than an uncontrolled system, requires a subtle balance of opposing effects, such as activation and inhibition, solute production and convection, or release and depletion of surfactants or electrolytes. This imposes limits on the parameter window where self-organization can be obtained (*e.g.* kinetic rate and diffusion constants, differences in density, surface tension, *etc.*). As a result, finding a new chemical system with a particular topology of feedback relations amongst chemical reactions and physicochemical principles that gives rise to self-organizing gradients is typically a serendipitous endeavour. And whereas moving particles driven by Marangoni flow or diffusiophoresis can easily be observed under the microscope (or even with the naked eye), reaction–diffusion or reaction–convection patterns that emerge in a homogeneous solution can easily be overlooked if the chemicals involved cannot be distinguished based on colour. In this regard, the development of DNA- and enzyme-based reaction networks – rather than exploiting reaction topologies of chemical systems that cannot be easily modified – opens new potential to follow a model-driven approach and design feedback relationships that can be implemented in the synthetic network topology. We note that the robustness and diversity of self-organizing modes can be expanded by combining different types of gradients – that are typically used in different physical environments, *e.g.* Marangoni flow with diffusiophoresis[172] or buoyancy.[91]

We anticipate that molecular systems which translate chemical reactions into gradients can strengthen the link between systems chemistry – *i.e.* the study of multicomponent molecular networks and their emergent properties – and advanced materials that operate at the micro-, meso- or macroscale.[173–175] Whereas classical responsive systems such as hydrogels typically respond to a single parameter (*e.g.* swelling/contraction upon pH change), sustained physicochemical gradients allow integration of multiple chemical input signals into a specific self-organizing response.[176,177] This might be exploited to direct the bottom-up construction of morphogenetic materials, for example in interactive biomaterials that adapt their form or texture in concert with biomolecular cues from the surrounding tissue. Alternatively, self-organization can generate read-out patterns in diagnostic systems that distinguish and report signal inputs derived from complex samples. Furthermore, in chemical systems that solve computational problems, such as maze-solving,[178] logic operations[179] or pattern recognition,[180] the information is typically transferred *via* diffusion among the 'computing cores' where chemical reactions take place that represent the computational steps. Whereas spread of molecular signals *via* diffusion by itself is uncontrolled, self-organizing gradients can autonomously determine how chemical input signals are guided, for example *via* reaction–diffusion waves, traveling droplets, growing filaments or organizing colloidal swarms, amongst the computing cores, and ultimately be transferred

into material-based responses. Taken together, we foresee that self-organization emerging from chemical systems presents new potential to process complex molecular information into matter-based functional behaviour.

Conflicts of interest

There are no conflicts of interest to declare.

Acknowledgements

We thank the Dutch Research Council (NWO, START-UP grant no. 740.018.003) as well as the Dutch Ministry of Education, Culture and Science (Gravitation program 024.001.035) for financial support.

References

1 G. M. Whitesides and B. Grzybowski, *Science*, 2002, **295**, 2418–2421.
2 P. Ball, *The Self-Made Tapestry: Pattern Formation in Nature*, Oxford University Press, Oxford, 2001.
3 T. Wittmann, A. Hyman and A. Desai, *Nat. Cell Biol.*, 2001, **3**, E28–E34.
4 A. Tero, S. Takagi, T. Saigusa, K. Ito, D. P. Bebber, M. D. Fricker, K. Yumiki, R. Kobayashi and T. Nakagaki, *Science*, 2010, **327**, 439–442.
5 T. Gregor, K. Fujimoto, N. Masaki and S. Sawai, *Science*, 2010, **328**, 1021–1025.
6 P. J. Keller, *Science*, 2013, **340**, 1234168.
7 G. Ashkenasy, T. M. Hermans, S. Otto and A. F. Taylor, *Chem. Soc. Rev.*, 2017, **46**, 2543–2554.
8 H. S. Azevedo, S. L. Perry, P. A. Korevaar and D. Das, *Nat. Chem.*, 2020, **12**, 793–794.
9 B. A. Grzybowski and W. T. S. Huck, *Nat. Nanotechnol.*, 2016, **11**, 585–592.
10 E. Mattia and S. Otto, *Nat. Nanotechnol.*, 2015, **10**, 111–119.
11 I. Prigogine and R. Lefever, *J. Chem. Phys.*, 1968, **48**, 1695–1700.
12 G. Nicolis and I. Prigogine, *Proc. Natl. Acad. Sci. U. S. A.*, 1981, **78**, 659–663.
13 G. Nicolis and I. Prigogine, *Self-Organization in Nonequilibrium Systems*, Wiley, New York, 1977.
14 L. Pismen, *Patterns and Interfaces in Dissipative Dynamics*, Springer Verlag Berlin, Heidelberg, 2006.
15 L. Onsager, *Phys. Rev.*, 1931, **37**, 405–426.
16 M. Kirschner and T. Mitchison, *Cell*, 1986, **45**, 329–342.
17 S. M. Morrow, I. Colomer and S. P. Fletcher, *Nat. Commun.*, 2019, **10**, 1–9.
18 K. K. Nakashima, J. F. Baaij and E. Spruijt, *Soft Matter*, 2018, **14**, 361–367.
19 G. Ragazzon and L. J. Prins, *Nat. Nanotechnol.*, 2018, **13**, 882–889.
20 E. te Brinke, J. Groen, A. Herrmann, H. A. Heus, G. Rivas, E. Spruijt and W. T. S. Huck, *Nat. Nanotechnol.*, 2018, **13**, 849–855.
21 J. Boekhoven, W. E. Hendriksen, G. J. M. Koper, R. Eelkema and J. H. van Esch, *Science*, 2015, **349**, 1075–1079.
22 M. Kumar, N. L. Ing, V. Narang, N. K. Wijerathne, A. I. Hochbaum and R. V. Ulijn, *Nat. Chem.*, 2018, **10**, 696–703.
23 A. Mishra, D. B. Korlepara, M. Kumar, A. Jain, N. Jonnalagadda, K. K. Bejagam, S. Balasubramanian and S. J. George, *Nat. Commun.*, 2018, **9**, 1–9.
24 R. K. Grötsch, C. Wanzke, M. Speckbacher, A. Angı, B. Rieger and J. Boekhoven, *J. Am. Chem. Soc.*, 2019, **141**, 9872–9878.
25 T. Heuser, E. Weyandt and A. Walther, *Angew. Chem., Int. Ed.*, 2015, **54**, 13258–13262.
26 A. M. Turing, *Philos. Trans. R. Soc., B*, 1952, **52**, 153–197.
27 L. Wolpert, *J. Theor. Biol.*, 1969, **25**, 1–47.
28 J. B. A. Green and J. Sharpe, *Development*, 2015, **142**, 1203–1211.
29 J. Briscoe and S. Small, *Development*, 2015, **142**, 3996–4009.
30 F. Brauns, G. Pawlik, J. Halatek, J. Kerssemakers, E. Frey and C. Dekker, *Nat. Commun.*, 2021, **12**, 1–11.
31 A. N. Landge, B. M. Jordan, X. Diego and P. Müller, *Dev. Biol.*, 2020, **460**, 2–11.
32 J. Halatek, F. Brauns and E. Frey, *Philos. Trans. R. Soc., B*, 2018, **373**, 20170107.
33 S. Kondo and T. Miura, *Science*, 2010, **329**, 1616–1620.
34 R. Sheth, L. Marcon, M. F. Bastida, M. Junco, L. Quintana, R. Dahn, M. Kmita, J. Sharpe and M. A. Ros, *Science*, 2014, **338**, 1476–1480.
35 A. D. Economou, A. Ohazama, T. Porntaveetus, P. T. Sharpe, S. Kondo, M. A. Basson, A. Gritli-Linde, M. T. Cobourne and J. B. A. Green, *Nat. Genet.*, 2012, **44**, 348–351.
36 V. Castets, E. Dulos, J. Boissonade and P. De Kepper, *Phys. Rev. Lett.*, 1990, **64**, 2953–2956.
37 I. Lengyel and I. R. Epstein, *Science*, 1991, **251**, 650–652.
38 I. Lengyel and I. R. Epstein, *Proc. Natl. Acad. Sci. U. S. A.*, 1992, **89**, 3977–3979.
39 K. Asakura, R. Konishi, T. Nakatani, T. Nakano and M. Kamata, *J. Phys. Chem. B*, 2011, **115**, 3959–3963.
40 K. J. Lee, W. D. McCormick, Q. Ouyang and H. L. Swinney, *Science*, 1993, **261**, 192–194.
41 K.-J. Lee, W. D. McCormick, J. E. Pearson and H. L. Swinney, *Nature*, 1994, **369**, 215–218.
42 I. Szalai and P. De Kepper, *Chaos*, 2008, **18**, 026105.
43 A. M. Zhabotinsky, *Biofizika*, 1964, **9**, 306–311.
44 A. N. Zaikin and A. M. Zhabotinsky, *Nature*, 1970, **225**, 535–537.
45 A. T. Winfree, *Science*, 1972, **175**, 634–636.
46 V. K. Vanag and I. R. Epstein, *Phys. Rev. Lett.*, 2001, **87**, 228301.
47 I. R. Epstein and V. K. Vanag, *Chaos*, 2005, **15**, 47510.
48 T. Bánsági, V. K. Vanag and I. R. Epstein, *Science*, 2011, **331**, 1309–1312.

49 V. K. Vanag and I. R. Epstein, *Chaos*, 2008, **18**, 026107.
50 J. E. Pearson, *Science*, 1993, **261**, 189–192.
51 V. K. Vanag and I. R. Epstein, *Phys. Chem. Chem. Phys.*, 2009, **11**, 897–912.
52 P. Gray and S. K. Scott, *Chem. Eng. Sci.*, 1984, **39**, 1087–1097.
53 A. Gierer and H. Meinhardt, *Kybernetik*, 1972, **12**, 30–39.
54 J. Schnakenberg, *J. Theor. Biol.*, 1979, **81**, 389–400.
55 R. J. Field and R. M. Noyes, *J. Chem. Phys.*, 1974, **60**, 1877–1884.
56 J. Horváth, I. Szalai and P. De Kepper, *Acc. Chem. Res.*, 2018, **51**, 3183–3190.
57 J. Horváth, I. Szalai and P. De Kepper, *Science*, 2009, **324**, 772–775.
58 Y. Kuramoto, *Chemical Oscillations, Waves and Turbulence*, Springer, Berlin, 1984.
59 I. R. Epstein and B. Xu, *Nat. Nanotechnol.*, 2016, **11**, 312–319.
60 V. K. Vanag and I. R. Epstein, *Proc. Natl. Acad. Sci. U. S. A.*, 2003, **100**, 14635–14638.
61 B. A. Grzybowski, *Chemistry in Motion: Reaction–Diffusion Systems for Micro- and Nanotechnology*, John Wiley & Sons, Ltd, Chichester, 2009.
62 M. Fialkowski, K. J. M. Bishop, R. Klajn, S. K. Smoukov, C. J. Campbell and B. A. Grzybowski, *J. Phys. Chem. B*, 2006, **110**, 2482–2496.
63 G. Ertl, *Science*, 1991, **254**, 1750–1755.
64 J. Wu, C. Yuan, T. Li, Z. Yuan, H. Zhang and X. Li, *J. Am. Chem. Soc.*, 2021, **143**, 13135–13144.
65 J. M. García-Ruiz, S. T. Hyde, A. M. Carnerup, A. G. Christy, M. J. Van Kranendonk and N. J. Welham, *Science*, 2003, **302**, 1194–1197.
66 J. M. García-Ruiz, E. Melero-García and S. T. Hyde, *Science*, 2009, **323**, 362–365.
67 P. Knoll, E. Nakouzi and O. Steinbock, *J. Phys. Chem. C*, 2017, **121**, 26133–26138.
68 P. Knoll and O. Steinbock, *Isr. J. Chem.*, 2018, **58**, 682–692.
69 W. L. Noorduin, A. Grinthal, L. Mahadevan and J. Aizenberg, *Science*, 2013, **340**, 832–837.
70 C. N. Kaplan, W. L. Noorduin, L. Li, R. Sadza, L. Folkertsma, J. Aizenberg and L. Mahadevan, *Science*, 2017, **355**, 1395–1399.
71 M. H. Bistervels, M. Kamp, H. Schoenmaker, A. M. Brouwer and W. L. Noorduin, *Adv. Mater.*, 2022, **34**, 2107843.
72 H. C. Hendrikse, A. van der Weijden, M. Ronda-Lloret, T. Yang, R. Bliem, N. R. Shiju, M. van Hecke, L. Li and W. L. Noorduin, *Adv. Mater.*, 2020, **32**, 1–7.
73 I. R. Epstein, V. K. Vanag, A. C. Balazs, O. Kuksenok, P. Dayal and A. Bhattacharya, *Acc. Chem. Res.*, 2012, **45**, 2160–2168.
74 O. Steinbock, V. Zykov and S. C. Müller, *Nature*, 1993, **366**, 322–324.
75 T. Sakurai, E. Mihaliuk, F. Chirila and K. Showalter, *Science*, 2002, **296**, 2009–2012.
76 R. Yoshida and T. Ueki, *NPG Asia Mater.*, 2014, **6**, e107.
77 S. Maeda, Y. Hara, R. Yoshida and S. Hashimoto, *Angew. Chem., Int. Ed.*, 2008, **47**, 6690–6693.
78 S. Maeda, Y. Hara, T. Sakai, R. Yoshida and S. Hashimoto, *Adv. Mater.*, 2007, **19**, 3480–3484.
79 X. Lu, L. Ren, Q. Gao, Y. Zhao, S. Wang, J. Yang and I. R. Epstein, *Chem. Commun.*, 2013, **49**, 7690–7692.
80 K. Torbensen, F. Rossi, S. Ristori and A. Abou-Hassan, *Lab Chip*, 2017, **17**, 1179–1189.
81 A. F. Taylor, M. R. Tinsley, F. Wang, Z. Huang and K. Showalter, *Science*, 2009, **323**, 614–617.
82 I. R. Epstein, *Chem. Commun.*, 2014, **50**, 10758–10767.
83 T. Litschel, M. M. Norton, V. Tserunyan and S. Fraden, *Lab Chip*, 2018, **18**, 714–722.
84 S. Chen and G. Seelig, *Soft Matter*, 2020, **16**, 3555–3563.
85 J. Zenk, D. Scalise, K. Wang, P. Dorsey, J. Fern, A. Cruz and R. Schulman, *RSC Adv.*, 2017, **7**, 18032–18040.
86 D. Scalise and R. Schulman, *Technology*, 2014, **02**, 55–66.
87 A. S. Zadorin, Y. Rondelez, G. Gines, V. Dilhas, G. Urtel, A. Zambrano, J. C. Galas and A. Estevez-Torres, *Nat. Chem.*, 2017, **9**, 990–996.
88 A. Senoussi, J. C. Galas and A. Estevez-Torres, *Sci. Adv.*, 2021, **7**, 1–10.
89 P. Glock, J. Broichhagen, S. Kretschmer, P. Blumhardt, J. Mücksch, D. Trauner and P. Schwille, *Angew. Chemie*, 2018, **130**, 2386–2390.
90 M. A. Budroni, F. Rossi and L. Rongy, *ChemSystemsChem*, 2022, **4**, e202100023.
91 M. A. Budroni, L. Rongy and A. De Wit, *Phys. Chem. Chem. Phys.*, 2012, **14**, 14619–14629.
92 A. De Wit, K. Eckert and S. Kalliadasis, *Chaos*, 2012, **22**, 37101.
93 I. Mutabazi, J. E. Wesfreid and E. Guyon, *Dynamics of Spatio-temporal Cellular Structures*, Springer, New York, 2006.
94 R. Tiani, A. De Wit and L. Rongy, *Adv. Colloid Interface Sci.*, 2018, **255**, 76–83.
95 D. Avnir and M. L. Kagan, *Chaos*, 1995, **5**, 589–601.
96 S. Chandrasekhar, *Hydrodynamic and Hydromagnetic Stability*, Oxford, Clarendon press, 1961.
97 D. Avnir and M. Kagan, *Nature*, 1984, **307**, 717–720.
98 I. Nagypal, G. Bazsa and I. R. Epstein, *J. Am. Chem. Soc.*, 1986, **108**, 3635–3640.
99 J. Masere, D. A. Vasquez, B. F. Edwards, J. W. Wilder and K. Showalter, *J. Phys. Chem.*, 1994, **98**, 6505–6508.
100 G. Bazsa and I. R. Epstein, *J. Phys. Chem.*, 1985, **89**, 3050–3053.
101 C. Almarcha, P. M. J. Trevelyan, P. Grosfils and A. De Wit, *Phys. Rev. Lett.*, 2010, **104**, 44501.
102 K. Eckert, M. Acker and Y. Shi, *Phys. Fluids*, 2003, **16**, 385–399.
103 V. Loodts, C. Thomas, L. Rongy and A. De Wit, *Phys. Rev. Lett.*, 2014, **113**, 114501.
104 R. K. Manna, K. Gentile, O. E. Shklyaev, A. Sen and A. C. Balazs, *Langmuir*, 2022, **38**, 1432–1439.
105 O. E. Shklyaev, V. V. Yashin, S. I. Stupp and A. C. Balazs, *Commun. Phys.*, 2020, **3**, 1–9.
106 Y. Zhang, S. Tsitkov and H. Hess, *Nat. Catal.*, 2018, **1**, 276–281.

107 M. A. Bees, A. J. Pons, P. G. Sørensen and F. Sagués, *J. Chem. Phys.*, 2001, **114**, 1932–1943.
108 K. Gentile, S. Maiti, A. Brink, B. Rallabandi, H. A. Stone and A. Sen, *Langmuir*, 2020, **36**, 7948–7955.
109 S. Sengupta, D. Patra, I. Ortiz-Rivera, A. Agrawal, S. Shklyaev, K. K. Dey, U. Córdova-Figueroa, T. E. Mallouk and A. Sen, *Nat. Chem.*, 2014, **6**, 415–422.
110 S. Maiti, O. E. Shklyaev, A. C. Balazs and A. Sen, *Langmuir*, 2019, **35**, 3724–3732.
111 I. Ortiz-Rivera, H. Shum, A. Agrawal, A. Sen and A. C. Balazs, *Proc. Natl. Acad. Sci. U. S. A.*, 2016, **113**, 2585–2590.
112 J. Leira-Iglesias, A. Tassoni, T. Adachi, M. Stich and T. M. Hermans, *Nat. Nanotechnol.*, 2018, **13**, 1021–1027.
113 E. Nakouzi and O. Steinbock, *Sci. Adv.*, 2016, **2**, e1601144.
114 L. M. Barge, S. S. S. Cardoso, J. H. E. Cartwright, G. J. T. Cooper, L. Cronin, A. De Wit, I. J. Doloboff, B. Escribano, R. E. Goldstein, F. Haudin, D. E. H. Jones, A. L. Mackay, J. Maselko, J. J. Pagano, J. Pantaleone, M. J. Russell, C. I. Sainz-Díaz, O. Steinbock, D. A. Stone, Y. Tanimoto and N. L. Thomas, *Chem. Rev.*, 2015, **115**, 8652–8703.
115 A. De Wit and G. M. Homsy, *J. Chem. Phys.*, 1999, **110**, 8663–8675.
116 L. A. Riolfo, Y. Nagatsu, S. Iwata, R. Maes, P. M. J. Trevelyan and A. De Wit, *Phys. Rev. E: Stat., Nonlinear, Soft Matter Phys.*, 2012, **85**, 15304.
117 Y. Nagatsu, K. Matsuda, Y. Kato and Y. Tada, *J. Fluid Mech.*, 2007, **571**, 475–493.
118 T. Podgorski, M. C. Sostarecz, S. Zorman and A. Belmonte, *Phys. Rev. E: Stat., Nonlinear, Soft Matter Phys.*, 2007, **76**, 16202.
119 F. Haudin, J. H. E. Cartwright, F. Brau and A. De Wit, *Proc. Natl. Acad. Sci. U. S. A.*, 2014, **111**, 17363–17367.
120 M. A. Budroni, V. Upadhyay and L. Rongy, *Phys. Rev. Lett.*, 2019, **122**, 244502.
121 A. A. Nepomnyashchy, M. G. Velarde and P. Colinet, *Interfacial Phenomena and Convection*, Chapman and Hall/CRC, New York, 2014.
122 A. S. Basu and Y. B. Gianchandani, *J. Micromech. Microeng.*, 2008, **18**, 115031.
123 T. Battal, C. D. Bain, M. Weiß and R. C. Darton, *J. Colloid Interface Sci.*, 2003, **263**, 250–260.
124 C. C. Maass, C. Krüger, S. Herminghaus and C. Bahr, *Annu. Rev. Condens. Matter Phys.*, 2016, **7**, 171–193.
125 R. Seemann, J.-B. Fleury and C. C. Maass, *Eur. Phys. J.: Spec. Top.*, 2016, **225**, 2227–2240.
126 N. J. Suematsu and S. Nakata, *Chem. – Eur. J.*, 2018, **24**, 6308–6324.
127 Y. Xu, N. Takayama, H. Er and S. Nakata, *J. Phys. Chem. B*, 2021, **125**, 1674–1679.
128 Y. Karasawa, T. Nomoto, L. Chiari, T. Toyota and M. Fujinami, *J. Colloid Interface Sci.*, 2018, **511**, 184–192.
129 Y. S. Ikura, R. Tenno, H. Kitahata, N. J. Suematsu and S. Nakata, *J. Phys. Chem. B*, 2012, **116**, 992–996.
130 Y. Karasawa, S. Oshima, T. Nomoto, T. Toyota and M. Fujinami, *Chem. Lett.*, 2014, **43**, 1002–1004.
131 S. Soh, K. J. M. Bishop and B. A. Grzybowski, *J. Phys. Chem. B*, 2008, **112**, 10848–10853.
132 L. J. Burton, N. Cheng and J. W. M. Bush, *Int. Comput. Biol.*, 2014, **54**, 969–973.
133 Y. Watahiki, T. Nomoto, L. Chiari, T. Toyota and M. Fujinami, *Langmuir*, 2018, **34**, 5487–5494.
134 M. Cheng, D. Zhang, S. Zhang, Z. Wang and F. Shi, *CCS Chem.*, 2019, **1**, 148–155.
135 I. Lagzi, S. Soh, P. J. Wesson, K. P. Browne and B. A. Grzybowski, *J. Am. Chem. Soc.*, 2010, **132**, 1198–1199.
136 K. Suzuno, D. Ueyama, M. Branicki, R. Tóth, A. Braun and I. Lagzi, *Langmuir*, 2014, **30**, 9251–9255.
137 A.-D. C. Nguindjel and P. A. Korevaar, *ChemSystemsChem*, 2021, **3**, e2100021.
138 B. A. Cicciarelli, T. A. Hatton and K. A. Smith, *Langmuir*, 2007, **23**, 4753–4764.
139 S. Chen, R. Costil, F. K.-C. Leung and B. L. Feringa, *Angew. Chem., Int. Ed.*, 2021, **60**, 11604–11627.
140 T. Shang, K. A. Smith and T. A. Hatton, *Langmuir*, 2003, **19**, 10764–10773.
141 A. Diguet, R.-M. Guillermic, N. Magome, A. Saint-Jalmes, Y. Chen, K. Yoshikawa and D. Baigl, *Angew. Chem., Int. Ed.*, 2009, **48**, 9281–9284.
142 C. Lv, S. N. Varanakkottu, T. Baier and S. Hardt, *Nano Lett.*, 2018, **18**, 6924–6930.
143 M. Schmitt and H. Stark, *Phys. Fluids*, 2016, **28**, 12106.
144 Y. Xiao, S. Zarghami, K. Wagner, P. Wagner, K. C. Gordon, L. Florea, D. Diamond and D. L. Officer, *Adv. Mater.*, 2018, **30**, 1801821.
145 Z. Izri, M. N. van der Linden, S. Michelin and O. Dauchot, *Phys. Rev. Lett.*, 2014, **113**, 248302.
146 S. Thutupalli, R. Seemann and S. Herminghaus, *New J. Phys.*, 2011, **13**, 73021.
147 D. Babu, R. J. H. Scanes, R. Plamont, A. Ryabchun, F. Lancia, T. Kudernac, S. P. Fletcher and N. Katsonis, *Nat. Commun.*, 2021, **12**, 2959.
148 D. Babu, N. Katsonis, F. Lancia, R. Plamont and A. Ryabchun, *Nat. Rev. Chem.*, 2022, **6**, 377–388.
149 S. I. Cheon, L. B. C. Silva, A. S. Khair and L. D. Zarzar, *Soft Matter*, 2021, **17**, 6742–6750.
150 A. van der Weijden, M. Winkens, S. M. C. Schoenmakers, W. T. S. Huck and P. A. Korevaar, *Nat. Commun.*, 2020, **11**, 1–10.
151 M. Winkens and P. A. Korevaar, *Langmuir*, 2022, **38**, 10799–10809.
152 C. H. Meredith, P. G. Moerman, J. Groenewold, Y. J. Chiu, W. K. Kegel, A. van Blaaderen and L. D. Zarzar, *Nat. Chem.*, 2020, **12**, 1136–1142.
153 N. J. Cira, A. Benusiglio and M. Prakash, *Nature*, 2015, **519**, 446–450.
154 Z. Li, H. Li, A. Li, Z. Liu, Z. Zhang, K. Li, Y. Qiao and Y. Song, *Adv. Mater. Interfaces*, 2021, **8**, 2101309.
155 D. Liu, A. Mahmood, D. Weng and J. Wang, *Langmuir*, 2019, **35**, 16146–16152.
156 M. Wittmann, M. N. Popescu, A. Domínguez and J. Simmchen, *Eur. Phys. J. E: Soft Matter Biol. Phys.*, 2021, **44**, 15.

157 S. Tanaka, S. Nakata and T. Kano, *J. Phys. Soc. Jpn.*, 2017, **86**, 101004.
158 J. Čejková, K. Schwarzenberger, K. Eckert and S. Tanaka, *Colloids Surf., A*, 2019, **566**, 141–147.
159 D. Velegol, A. Garg, R. Guha, A. Kar and M. Kumar, *Soft Matter*, 2016, **12**, 4686–4703.
160 Y. Peng, P. Xu, S. Duan, J. Liu, J. L. Moran and W. Wang, *Angew. Chem., Int. Ed.*, 2022, **61**, e202116041.
161 W. Wang, W. Duan, S. Ahmed, A. Sen and T. E. Mallouk, *Acc. Chem. Res.*, 2015, **48**, 1938–1946.
162 A. Banerjee and T. M. Squires, *Sci. Adv.*, 2019, **5**, eaax1893.
163 J. J. McDermott, A. Kar, M. Daher, S. Klara, G. Wang, A. Sen and D. Velegol, *Langmuir*, 2012, **28**, 15491–15497.
164 R. Niu, T. Palberg and T. Speck, *Phys. Rev. Lett.*, 2017, **119**, 028001.
165 R. Niu, A. Fischer, T. Palberg and T. Speck, *ACS Nano*, 2018, **12**, 10932–10938.
166 I. Theurkauff, C. Cottin-Bizonne, J. Palacci, C. Ybert and L. Bocquet, *Phys. Rev. Lett.*, 2012, **108**, 268303.
167 A. Bricard, J. B. Caussin, N. Desreumaux, O. Dauchot and D. Bartolo, *Nature*, 2013, **503**, 95–98.
168 W. Duan, R. Liu and A. Sen, *J. Am. Chem. Soc.*, 2013, **135**, 1280–1283.
169 M. Ibele, T. E. Mallouk and A. Sen, *Angew. Chem., Int. Ed.*, 2009, **48**, 3308–3312.
170 A. Altemose, M. A. Sánchez-Farrán, W. Duan, S. Schulz, A. Borhan, V. H. Crespi and A. Sen, *Angew. Chemie*, 2017, **129**, 7925–7929.
171 C. Wu, J. Dai, X. Li, L. Gao, J. Wang, J. Liu, J. Zheng, X. Zhan, J. Chen, X. Cheng, M. Yang and J. Tang, *Nat. Nanotechnol.*, 2021, **16**, 288–295.
172 P. Bacchin, K. Glavatskiy and V. Gerbaud, *Phys. Chem. Chem. Phys.*, 2019, **21**, 10114–10124.
173 H. W. H. van Roekel, B. J. H. M. Rosier, L. H. H. Meijer, P. A. J. Hilbers, A. J. Markvoort, W. T. S. Huck and T. F. A. de Greef, *Chem. Soc. Rev.*, 2015, **44**, 7465–7483.
174 R. Merindol and A. Walther, *Chem. Soc. Rev.*, 2017, **46**, 5588–5619.
175 B. A. Grzybowski, K. Fitzner, J. Paczesny and S. Granick, *Chem. Soc. Rev.*, 2017, **46**, 5647–5678.
176 C. Kaspar, B. J. Ravoo, W. G. van der Wiel, S. V. Wegner and W. H. P. Pernice, *Nature*, 2021, **594**, 345–355.
177 A. Walther, *Adv. Mater.*, 2020, **32**, 1905111.
178 O. Steinbock, Á. Tóth and K. Showalter, *Science*, 1995, **267**, 868–871.
179 O. Steinbock, P. Kettunen and K. Showalter, *J. Phys. Chem.*, 1996, **100**, 18970–18975.
180 J. M. Parrilla-Gutierrez, A. Sharma, S. Tsuda, G. J. T. Cooper, G. Aragon-Camarasa, K. Donkers and L. Cronin, *Nat. Commun.*, 2020, **11**, 1442.